Chapter 6

Effect of Magnetism on the Barrier Height

6.1 Introduction

One of the characteristic features of perovskite oxides is the abundance of magnetic ground states present [1]. Among the materials with *ferromagnetic* ground states, perovskites including manganese are attracting significant attention for their high Curie temperature and the strong coupling of the ferromagnetic ground state to the electrical properties, making them potential candidates for magnetic devices [2–4]. The physics of manganites is complex due to the similar energy scales involved in the interactions between structural, electronic and magnetic degrees of freedom. The magnetic interactions have been based on the double exchange interaction between Mn-O-Mn nearest neighbors [5, 6] and the strong coupling with the lattice in connection with the Jahn-Teller distortion of the Mn-O octahedra [7]. The most significant property of the manganites is the so called *colossal magnetoresistance (CMR)*, which is the large negative magnetoresistance exhibited close to T_C as seen in Sr or Ca doped $LaMnO_3$ shown in Fig. 6.1 [8]. The robust crystal structure of the perovskite enables different A-site cation occupation in manganites. The magnetic and the electronic phase diagram of four such examples of A-site cation combination are shown in Fig. 6.2. It is evident that the conductivity, magnetic ground states and the ordering temperatures can be tuned by specifying the desired A-site cation and the stoichiometry.

After the success in fabrication of manganites in thin film form [11], research on interfaces using manganites has accelerated by strong motivation to fabricate devices. The field investigated most significantly is in magnetic tunneling junctions [12–14], taking advantage of the fully spin-polarized ground state in $La_{0.7}Sr_{0.3}MnO_3$. Recently there has also been emerging interest in more fundamental building blocks such as *pn-* or *pin-* junctions [15, 16] and in Schottky junctions, with motivations to demonstrate the bulk magnetic properties in junction structures. Examples include $La_{1-x}Sr_xMnO_3$ [17, 18], $La_{1-x}Ca_xMnO_3$ [19] or $La_{1-x}Ce_xMnO_3$ [20, 21]. The majority of the measurements in these junctions are I-V characteristics which show device operation with characteristic features of the bulk manganites as a function

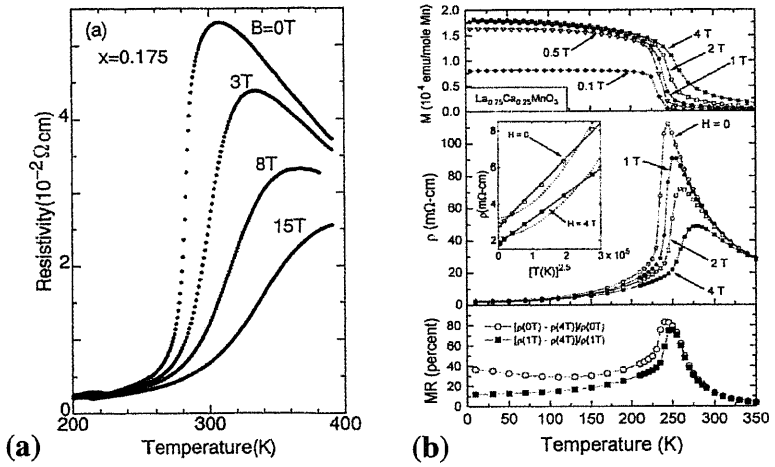

Figure 6.1: Temperature dependence of the resistivity under applied magnetic field in (a) $La_{1-x}Sr_xMnO_3$ (x = 0.175) [8] and (b) $La_{0.75}Ca_{0.25}MnO_3$ together with magnetization and magnetoresistance [9].

of temperature or magnetic fields. However, in order to understand the characteristic features evidenced in I-V or other junction characterizations, it is essential that the band alignment at the interface is understood. The importance of interface band alignment and its sensitivity to magnetism has already been pointed out in the major fields of spintronic devices in other material systems.

In the studies of electrical injection of highly polarized spins in Schottky junctions using ferromagnetic metals [22–24] or heterojunctions between a non-magnetic semiconductor and dilute magnetic semiconductors (DMS) [25–28], it has been known that the injection efficiency is very sensitive to the interface barrier formation [29–31]. For example, a substantial difference in the SBH is expected by changing the surface termination of GaAs in Fe/GaAs Schottky junction, influencing the spin injection efficiency [31]. Also the coupling of magnetism and junction properties at the interface can be seen in spin selective heterostructures. A metal-insulator-metal tunneling junction with europium chalcogenide as the insulator has shown a large magnetic field sensitivity in the tunneling current [32], which later proved to be due to the change in the built-in potential existing from spin ordering of the $4f$ electrons [33]. Similar experiments using DMS has been done in Au/n-$Cd_{1-x}Mn_xSe$ [34] or Au/n-$Cd_{1-x}Mn_xTe$ [35] Schottky junctions producing suggestive evidence of built-in potential change induced by magnetic field. However the origin of the field induced barrier change has not been understood solely by the bulk magnetic properties of the semiconductors.

Most of the studies in spintronics have used well established conventional semiconductors as part of their structures. In the case of manganite based junctions, the strong interaction between the many degrees of freedom makes them a challenging system to investigate for the various possible effects on the interface electronic structures.

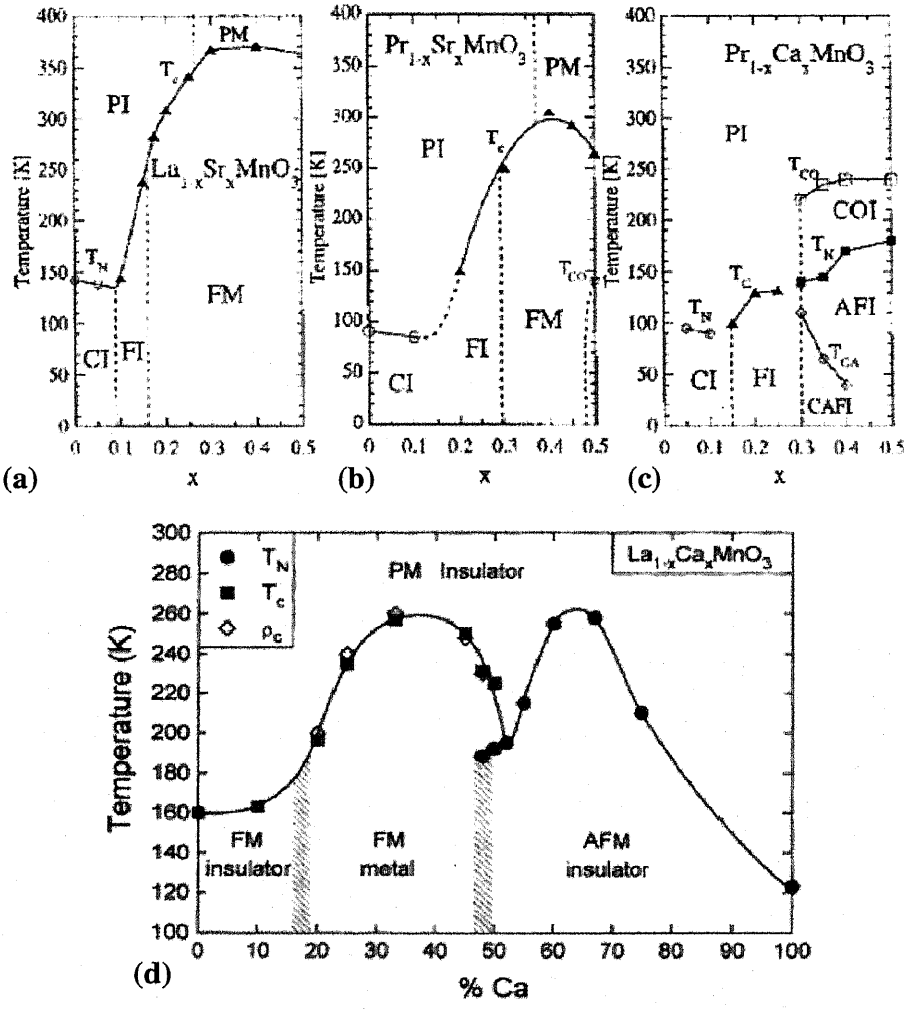

Figure 6.2: Magnetic and electronic phase diagram versus x for (a) $La_{1-x}Sr_xMnO_3$, (b) $Pr_{1-x}Sr_xMnO_3$, (c) $Pr_{1-x}Ca_xMnO_3$ [8] and (d) $La_{1-x}Ca_xMnO_3$ [9]. Abbreviations: F - ferromagnetic, P - paramagnetic, AF - antiferromagnetic, C - canted magnetic structure, T_C - ferromagnetic Curie temperature, T_N - Neel temperature, M - metal, I - insulator and CO - charge ordered phase.

A suitable model system is required to investigate the effect of magnetism at the interface. From recent reports, we focus our study in the system $La_{0.7}Sr_{0.3}MnO_{3-\delta}$ /Nb:$SrTiO_3$ in which large magnetic field dependence in the forward bias current is observed (Fig. 6.3) [17]. The absence of the effect in $La_{0.7}Sr_{0.3}MnO_3$ raises the question of the role of oxygen deficiency in $La_{0.7}Sr_{0.3}MnO_{3-\delta}$. The temperature dependence of the effect can be seen in the plot of the dc-conductance and the zero-bias capacitance shown in Fig. 6.4. The exponential decrease in the dc-conductance

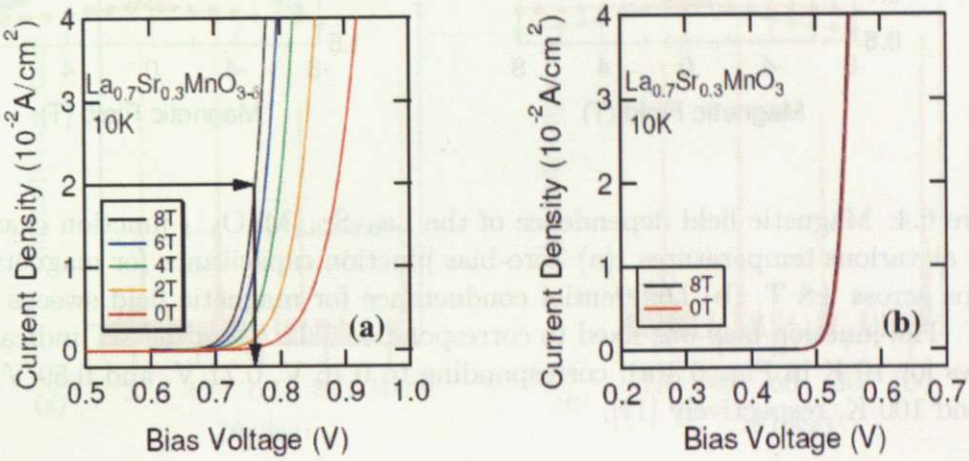

Figure 6.3: (a) Magnetic field dependence of the $La_{0.7}Sr_{0.3}MnO_{3-\delta}$ junction forward bias characteristics at 10 K. (b) Magnetic field dependence of the $La_{0.7}Sr_{0.3}MnO_3$ junction forward bias characteristics at 10 K [17].

and the linear decrease in the zero-bias capacitance both suggest a reduction in the depletion width, on the assumption that the current transport process is FE and the measured capacitance is the depletion capacitance. However, as in many cases, the junction characterization through I-V or C-V always involve application of bias voltage which hinders the extraction of the physical parameters at thermal equilibrium.

6.2 Motivation

In this study, we investigate the magnetic field sensitive Schottky junction in $La_{0.7}Sr_{0.3}MnO_{3(-\delta)}$/Nb:$SrTiO_3$, making it a potential candidate device element for magnetic field sensitive transistors or magnetic field sensors. The study is aimed at clarifying the physical origin of the magnetic field dependence in the junction and gain insights for effective methods to design heterostructures for functionalities coupled to magnetic field. Internal photoemission is used to determine the SBH at thermal equilibrium which is compared with other measurements to understand the detailed band diagram of the system.

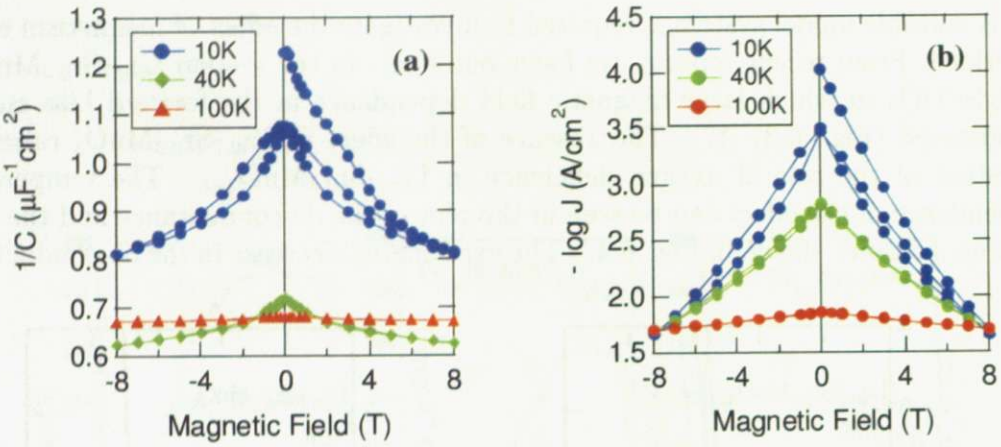

Figure 6.4: Magnetic field dependence of the $La_{0.7}Sr_{0.3}MnO_{3-\delta}$ junction characteristics at various temperatures. (a) Zero-bias junction capacitance for magnetic field sweeps across ±8 T. (b) Differential conductance for magnetic field sweeps across ±8 T. The junction bias was fixed to correspond to 0.02 A/cm^2 at 8 T indicated by arrows for 10 K in Fig. 6.3(a), corresponding to 0.76 V, 0.71 V, and 0.59 V at 10, 40, and 100 K, respectively [17].

6.3 Experimental

Table 6.1: Growth conditions for the $La_{0.7}Sr_{0.3}MnO_{3(-\delta)}$/Nb:$SrTiO_3$ Schottky junctions.

	$La_{0.7}Sr_{0.3}MnO_3$	$La_{0.7}Sr_{0.3}MnO_{3-\delta}$
Substrate	Nb:$SrTiO_3$ Nb = 0.01 wt%	
Oxygen Partial Pressure (Torr)	250	1.0
Substrate Temperature (°C)	750	
Laser Fluency (J/cm^2)	4.0	

The junctions were fabricated by the PLD method under the conditions shown in Table 6.1, which are the same as those reported by Nakagawa *et al.* [17]. The electrical contacts for the junctions were made by using silver epoxy paint (Epotek) and ultrasonic solder for the $La_{0.7}Sr_{0.3}MnO_{3(-\delta)}$ and Nb:$SrTiO_3$, respectively. For in-plane transport measurements, silver epoxy was used to make four contacts onto the film surface.

Measurements of I-V, C-V and IPE were conducted inside a liquid helium cryostat (Physical Property Measurement System, Quantum Design). Unless stated otherwise, the magnetic field was applied perpendicular to the junction surface in all the measurements.

6.4 Results and Discussions

6.4.1 Thin Film Characterization

The lattice constants of $La_{0.7}Sr_{0.3}MnO_{3-\delta}$ was determined from X-ray 2θ-θ diffraction (XRD) measurements shown in Figs. 6.5 and 6.6. The absence of diffrac-

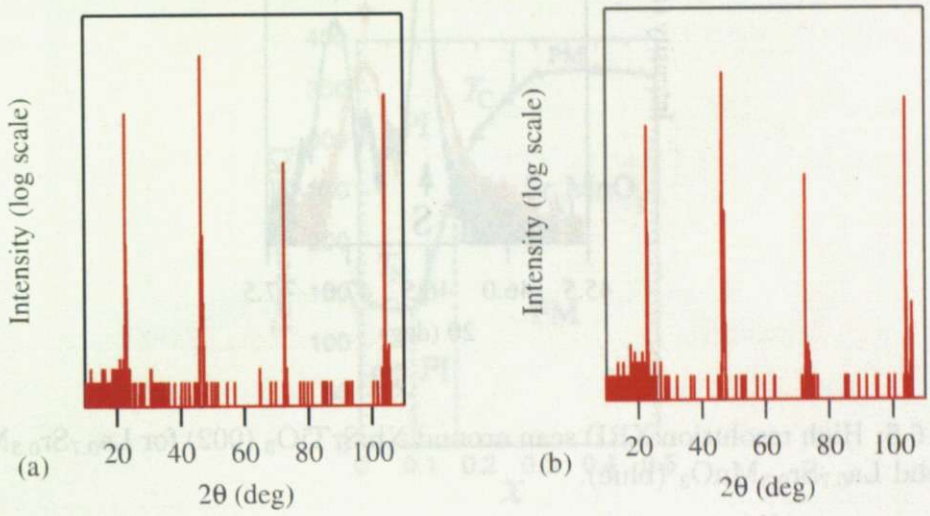

Figure 6.5: Wide range XRD spectra for (a) $La_{0.7}Sr_{0.3}MnO_{3-\delta}$ and (b) $La_{0.7}Sr_{0.3}MnO_3$. The peaks correspond to the Nb:$SrTiO_3$ $(00n)$, showing the epitaxial growth of the $La_{0.7}Sr_{0.3}MnO_{3(-\delta)}$ films.

tion peaks other than $(00n)$, corresponding to those perpendicular to the surface of the substrates, indicates the epitaxial growth of the films and the absence of secondary phase formation. From the high resolution measurements around the (002) peak, the out-of-plane lattice constants of the films are estimated to be 3.872 Å($La_{0.7}Sr_{0.3}MnO_3$) and 3.858 Å($La_{0.7}Sr_{0.3}MnO_{3-\delta}$). Since the c-axis lattice constant of $La_{0.7}Sr_{0.3}MnO_3$ single crystal is reported to be 3.889 Å [36], both films on $SrTiO_3$ substrates are contracted in the out-of-plane direction. Notice that the out-of-plane lattice constant for $La_{0.7}Sr_{0.3}MnO_{3-\delta}$ is smaller by 0.36% than that of $La_{0.7}Sr_{0.3}MnO_3$, implying the stronger tensile strain in $La_{0.7}Sr_{0.3}MnO_{3-\delta}$.

$La_{0.7}Sr_{0.3}MnO_3$ films were deposited simultaneously on $SrTiO_3(001)$ substrates under the same conditions as those on Nb:$SrTiO_3$. The resistivity of the films are shown in Fig. 6.7(a). The peak temperature in ρ-T is reduced by $\sim$ 60K from $\sim$ 340K for $La_{0.7}Sr_{0.3}MnO_3$ to $\sim$ 280K for $La_{0.7}Sr_{0.3}MnO_{3-\delta}$. The resistivity measured under applied magnetic field of 6 T revealed a change in the resistivity similar to the behavior reported in Ref. [17] where a larger magnetoresistance was observed for $La_{0.7}Sr_{0.3}MnO_{3-\delta}$ compared with $La_{0.7}Sr_{0.3}MnO_3$. The reduced peak temperature from $\rho-T$ is consistent with the reduced Curie temperature determined from the magnetization measurement carried out using a SQUID magnetometer shown in Fig. 6.7(b). To first approximation, the reduced Curie temperature in $La_{0.7}Sr_{0.3}MnO_{3-\delta}$ can be interpreted as reduction in the hole concentration, which

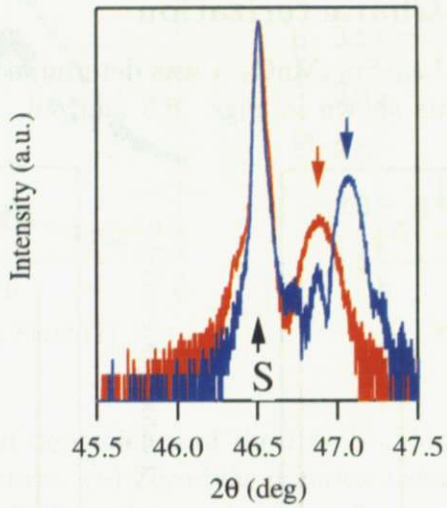

Figure 6.6: High resolution XRD scan around Nb:$SrTiO_3$ (002) for $La_{0.7}Sr_{0.3}MnO_{3-\delta}$ (red) and $La_{0.7}Sr_{0.3}MnO_3$ (blue).

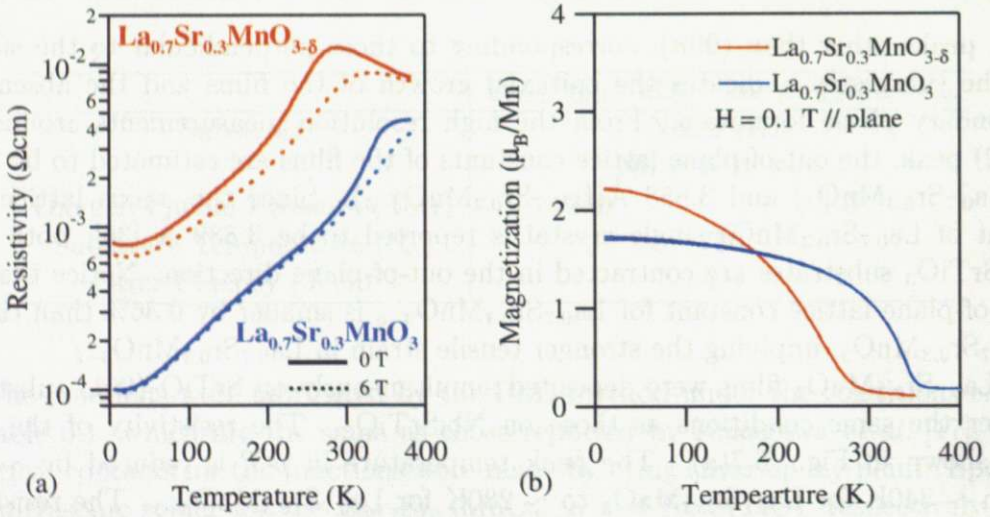

Figure 6.7: (a) Resistivity and (b) magnetization of $La_{0.7}Sr_{0.3}MnO_3$ (blue lines) and $La_{0.7}Sr_{0.3}MnO_{3-\delta}$ (red lines) under applied magnetic field of 0 T (solid lines) and 6 T (dotted lines).

enables us to estimate the hole concentration in $La_{0.7}Sr_{0.3}MnO_{3-\delta}$ from the magnetic phase diagram of $La_{1-x}Sr_xMnO_3$ (Fig. 6.8) [37]. Assuming the valency of lanthanum as La^{3+} and of oxygen as O^{2-}, the hole concentration of $La_{1-x}Sr_xMnO_{3-\delta}$ on the Mn site is $x - 2\delta$. From Fig. 6.8, the hole concentration corresponding to a T_C of 280 K is $x = 0.175$ which gives us an estimate for the oxygen deficiency of $\delta \sim 0.06$ from $0.3 - 2\delta \sim 0.175$.

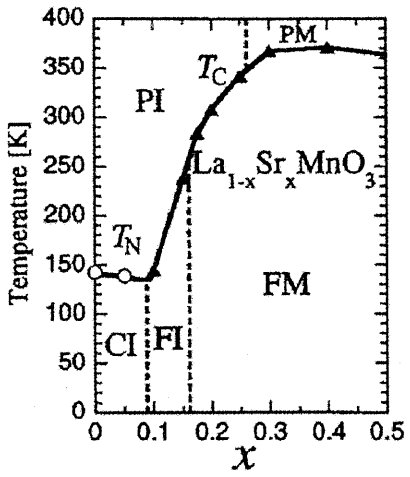

Figure 6.8: Magnetic and electronic phase diagram of $La_{1-x}Sr_xMnO_3$ [37].

6.4.2 General Junction Characterization

I-V Characteristics

The temperature dependence of rectifying $La_{0.7}Sr_{0.3}MnO_{3(-\delta)}$/Nb:$SrTiO_3$ junctions measured under zero magnetic field is shown in Fig. 6.9(a) and (b). A shift in the onset voltage of the forward bias current is seen with decrease in temperature for both junctions. The semi-logarithmic plot shown in Figs. 6.9(c) and (d) demonstrate the linear voltage dependence of the forward bias current and their evolution with temperature. A systematic decrease in the reverse bias current J_R, which is independent of voltage, is seen in both junctions above $\sim$ 100 K, below which an increase in the J_R is seen as the temperature is decreased. The low temperature J_R shows a large voltage dependence which differs from the high temperature reverse bias current. Comparison of the low temperature reverse bias current is shown in Fig. 6.10 for $La_{0.7}Sr_{0.3}MnO_3$ and $La_{0.7}Sr_{0.3}MnO_{3-\delta}$ at 10 and 50 K. The voltage dependence of it has been given many explanations such as: Zener tunneling, impact ionization breakdown, image force lowering, etc. Among the various voltage dependences often observed at interfaces and bulk conduction in insulators, the voltage dependence in the case of $La_{0.7}Sr_{0.3}MnO_{3-\delta}$ can be fitted satisfactorily with the Poole-Frenkel emission formula

$$J \sim V \exp(a\sqrt{V}/T). \tag{6.1}$$

The smaller current at higher temperature is also consistent with Eq. (6.1). The Poole-Frenkel emission process is likely to be dominating at 10 K for $La_{0.7}Sr_{0.3}MnO_3$, however it is interesting that the identical formula does not apply at 50 K implying the possible presence of different conduction process.

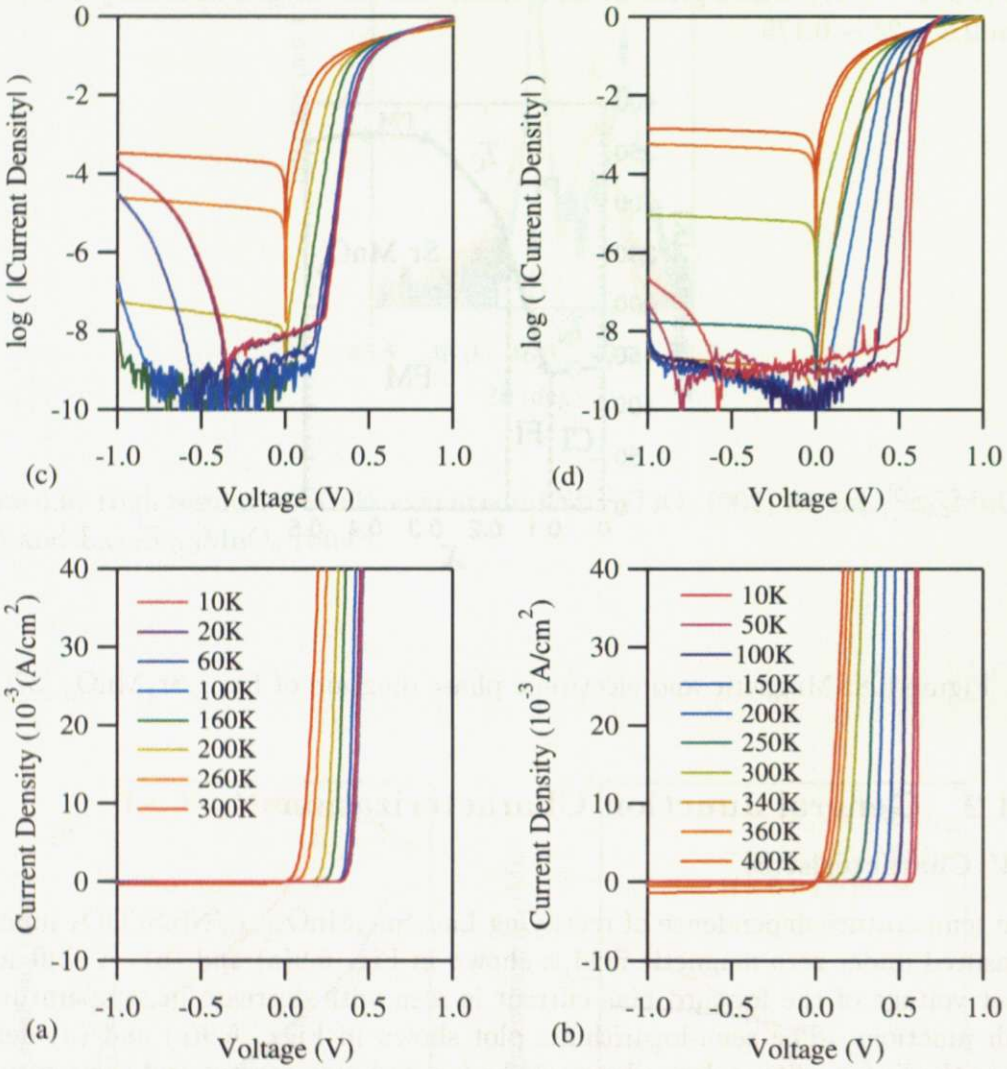

Figure 6.9: Temperature dependent I-V characteristics for (a) $La_{0.7}Sr_{0.3}MnO_{3-\delta}$ and (b) $La_{0.7}Sr_{0.3}MnO_3$ in linear scale. Semi logarithmic plot shown in (c) and (d) respectively.

Another possibility for the J_R behavior at low temperatures is the effect of the electric field dependent permittivity in $SrTiO_3$. The decrease in the dielectric permittivity at the interface by the electric field narrows the depletion width resulting in a higher tunneling probability. Using the SBH obtained from the IPE measurements and a nominal value for N_D in Nb:$SrTiO_3$, the calculated electric field at the interface, E_{max}, and the depletion widths at various reverse bias voltages are shown in Fig. 6.11. It is apparent that the effect of reverse bias voltage on E_{max}

is strongly enhanced as the temperature is reduced. The bias voltage effect on the total depletion width is small at low temperatures where tunneling is more likely. Approximating the reverse biased band bending as a triangular potential, the tunneling probability is estimated to be $P \propto \exp(-1/E_{max})$ from Eq.(3.33), which indicates that higher electric fields give higher tunneling probability.

It is not certain whether or both the Poole-Frenkl or the permittivity effect are dominating process of J_R, since no functional formula is available for FE process in Schottky junctions incorporating the effect of electric field dependent permittivity.

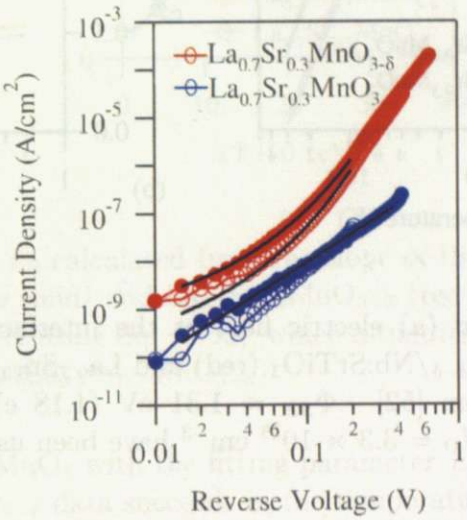

Figure 6.10: I-V characteristics at reverse bias in $La_{0.7}Sr_{0.3}MnO_{3-\delta}$ and $La_{0.7}Sr_{0.3}MnO_3$ measured at 10 K (closed circles), 50 K (open circles). The data have been shifted so as to set the onset of the current at V = 0.

Based on the assumption of a thermoionic emission process across the junction, the SBH and the ideality factor n is determined from Eq. (3.31) in Fig. 6.12.

$$J = A^* T^2 \exp\left(-\frac{q\Phi_B}{kT}\right) \exp\left(\frac{qV}{nkT}\right) \tag{6.2}$$

Here we set the effective Richardson constant A^* to be 156 Acm^{-2}K^{-2}, which corresponds to the effective mass $m^* = 1.3m_0$ for Nb:$SrTiO_3$ [38]. The extracted SBH decreases with decrease in temperature with a change in the slope between 60 < T < 100 K. This implies the disappearance of the barrier heights with decrease in temperature, which is inconsistent with the rectifying behavior observed even at the lowest temperature (Fig. 6.9). This is a clear indication that the transport process other than TE should be dominant at low temperatures. One obvious candidate is the TFE or FE process. In order to determine the dominance of these processes, E_0, a measure of field emission contribution in I-V, was calculated from the ideality factors for each temperature using the relation $E_0 = nkT/q$. The relation between E_0 and the thermal energy are plotted in Fig. 6.13. Fitting to the experimental data using Eq.(3.38) are shown as dotted lines. A relatively good agreement is obtained

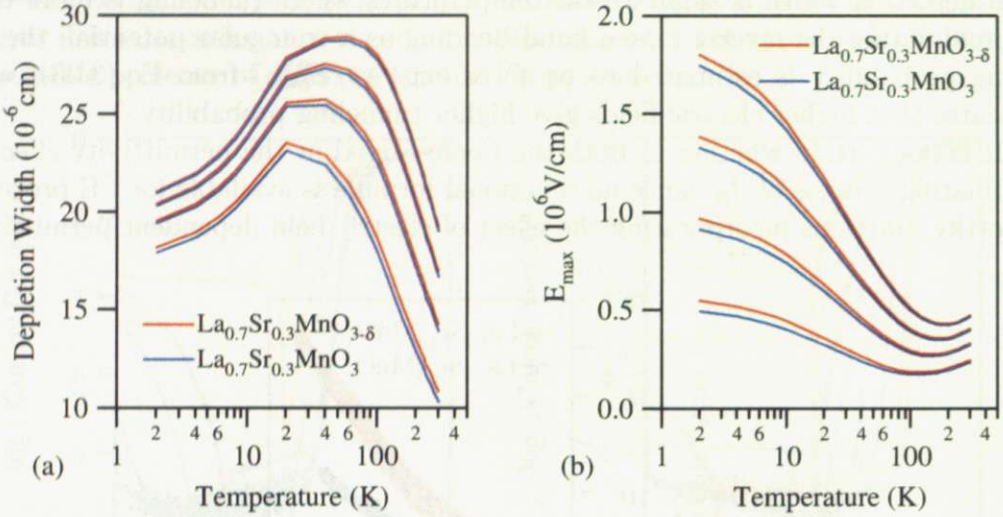

Figure 6.11: Calculated (a) electric field at the interface and (b) the depletion width in $La_{0.7}Sr_{0.3}MnO_{3-\delta}$/Nb:$SrTiO_3$ (red) and $La_{0.7}Sr_{0.3}MnO_3$/Nb:$SrTiO_3$ (blue) based on equations from [52]. Φ_{SB} = 1.31 eV (1.18 eV) for $La_{0.7}Sr_{0.3}MnO_{3-\delta}$ ($La_{0.7}Sr_{0.3}MnO_3$) and $N_D = 3.3 \times 10^{18}$ cm^{-3} have been used as input parameters.

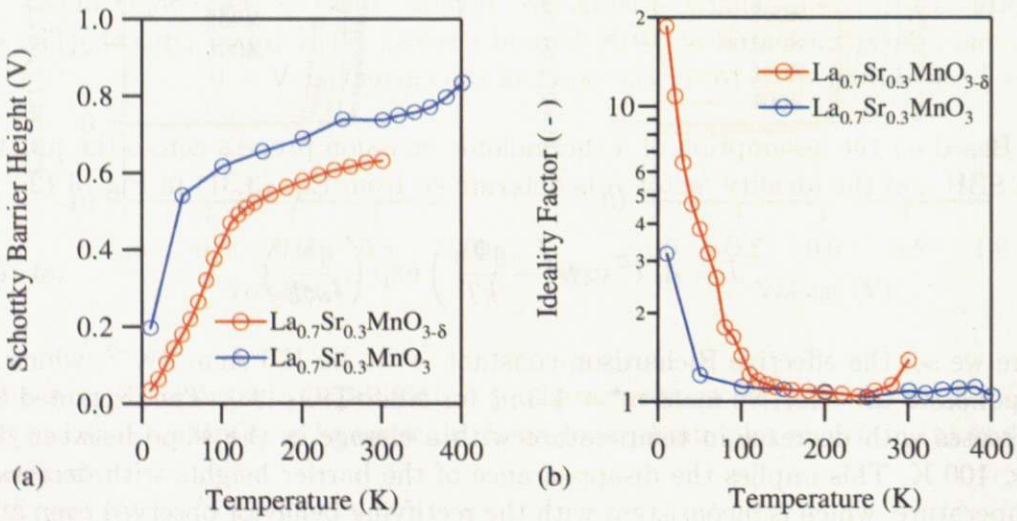

Figure 6.12: (a) Schottky barrier heights and (b) the ideality factor n deduced from I-V characteristics based on the thermoionic emission model for $La_{0.7}Sr_{0.3}MnO_3$ (blue) and $La_{0.7}Sr_{0.3}MnO_{3-\delta}$ (red). Decrease in the barrier height with decrease in temperature is observed in both junctions.

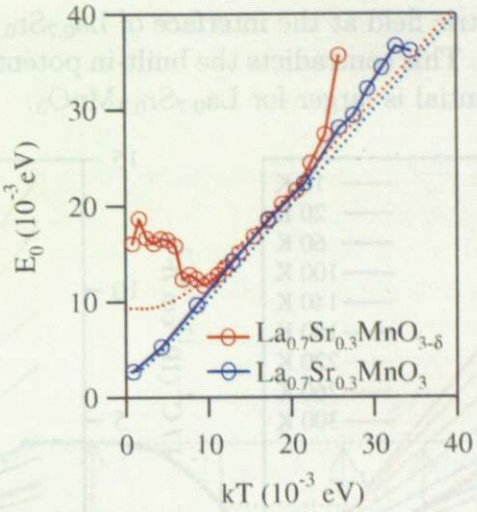

Figure 6.13: Parameter E_0 calculated from the slope of the I-V curves in Fig..6.9 for $La_{0.7}Sr_{0.3}MnO_3$ (blue solid) and $La_{0.7}Sr_{0.3}MnO_{3-\delta}$ (red solid). The dotted lines represent the fitting curves using Eq. (3.38), which estimates values of $E_{00} = 2.7(9.3)$ meV for $La_{0.7}Sr_{0.3}MnO_3$ ($La_{0.7}Sr_{0.3}MnO_{3-\delta}$).

in the case of $La_{0.7}Sr_{0.3}MnO_3$ with the fitting parameter $E_{00} = 2.7$ meV. Attempts to fit the $La_{0.7}Sr_{0.3}MnO_{3-\delta}$ data succeeds in the temperature range between 100 K and 250 K, but fails to explain the behavior at lower temperatures. The best fit using $E_{00} = 9.9$ meV predicts a saturation below ~ 37 K, but E_0 shows an upturn which is unexpected even for TFE or FE. Therefore we can conclude that the high temperature current transport process is likely to be TFE but the low temperature characteristics in $La_{0.7}Sr_{0.3}MnO_{3-\delta}$ cannot be explained by a simple FE process. Similar analysis carried out by Susaki *et al.* [39] have presented evidence of crossover from TFE to FE behavior in *both* of these junctions. The differences between Ref. [39] and the present data are suspected to be due to the difference in the subtle growth conditions or the differences in the fitting region for estimating the ideality factors.

From the temperature dependence of the I-V characteristics, we have found that the transport process is dominated by TFE in the high temperature region and at low temperatures, evidence for non-trivial additional current transport process have been found.

C-V Characteristics

The temperature dependence of C-V characteristics are shown in Fig. 6.14 for $La_{0.7}Sr_{0.3}MnO_{3-\delta}$ and $La_{0.7}Sr_{0.3}MnO_3$. The built-in potentials were estimated by fitting the C^{-2}-V with Eq. (5.7) for low temperatures ($T < 200$ K)and Eq. (3.61) for high temperatures ($T > 200$ K). In the case of Eq. (5.7), the curves were fitted by using three free parameters, namely the built-in potential V_{bi} and the two prefactors in the linear and the quadratic terms. The curved behavior in Fig. 6.14(a) indicates

a stronger internal electric field at the interface of $La_{0.7}Sr_{0.3}MnO_{3-\delta}$ compared with that of $La_{0.7}Sr_{0.3}MnO_3$. This contradicts the built-in potential results in Fig. 6.14(c) where the built-in potential is larger for $La_{0.7}Sr_{0.3}MnO_3$.

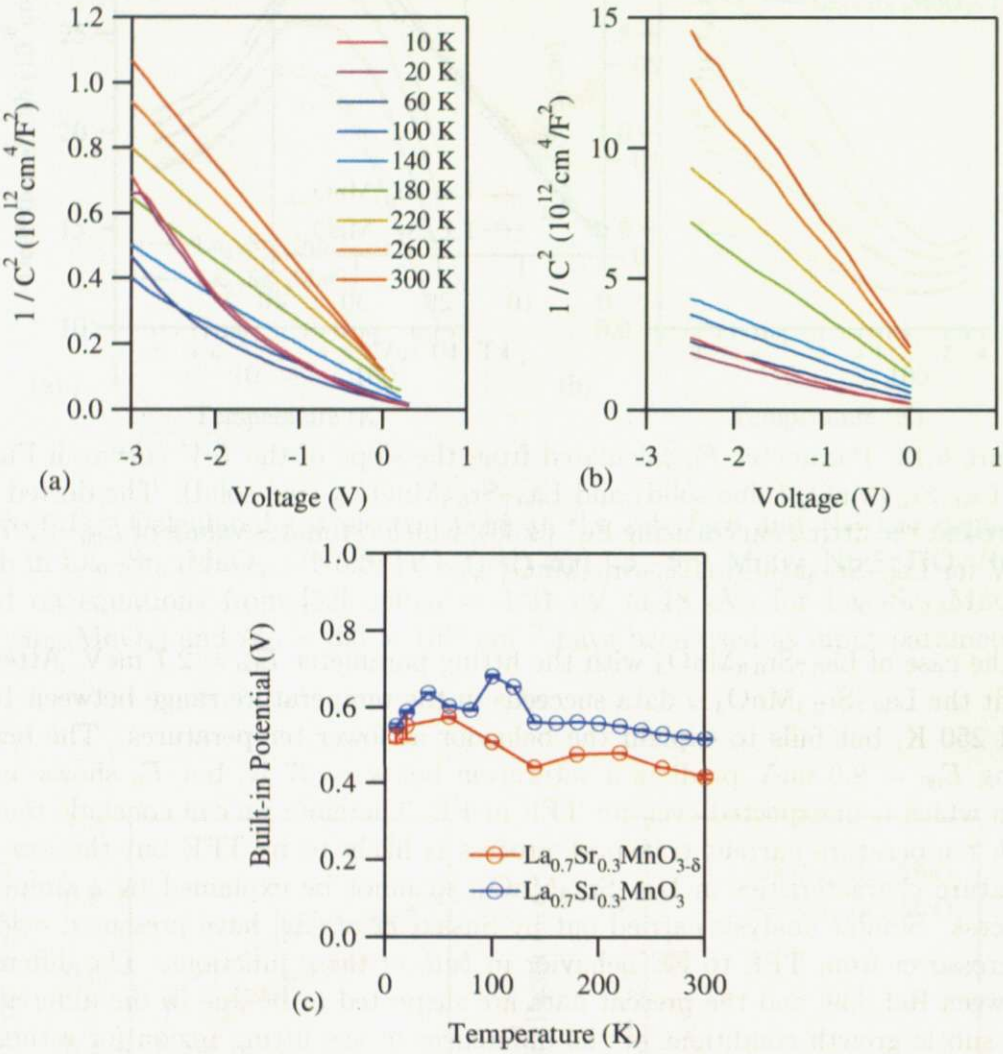

Figure 6.14: Temperature dependence of the C-V characteristics for (a) $La_{0.7}Sr_{0.3}MnO_{3-\delta}$ and (b) $La_{0.7}Sr_{0.3}MnO_3$ and (c) the estimated built-in potentials.

One possible reason could be that the assumption of *Schottky* junctions in $La_{0.7}Sr_{0.3}MnO_{3-\delta}$ is not justified. As we have estimated from the reduced T_C, a *pn* heterojunction may be a better starting point for the analysis of C-V in the case of $La_{0.7}Sr_{0.3}MnO_{3-\delta}$. By considering $La_{0.7}Sr_{0.3}MnO_{3-\delta}$/Nb:$SrTiO_3$ as a *pn* heterojunction, we expect a contribution in the depletion capacitance from the $La_{0.7}Sr_{0.3}MnO_{3-\delta}$ side similar to the case proposed by Anderson in Ge/GaAs [40]. The Anderson model of band alignment at semiconductor-semiconductor interface is based on the assumption of direct contact with no interface states, similar to the Schottky-Mott model in metal-semiconductor contacts. The apparent built-in potential measured by C-V is the sum of the built-in potentials on $La_{0.7}Sr_{0.3}MnO_{3-\delta}$

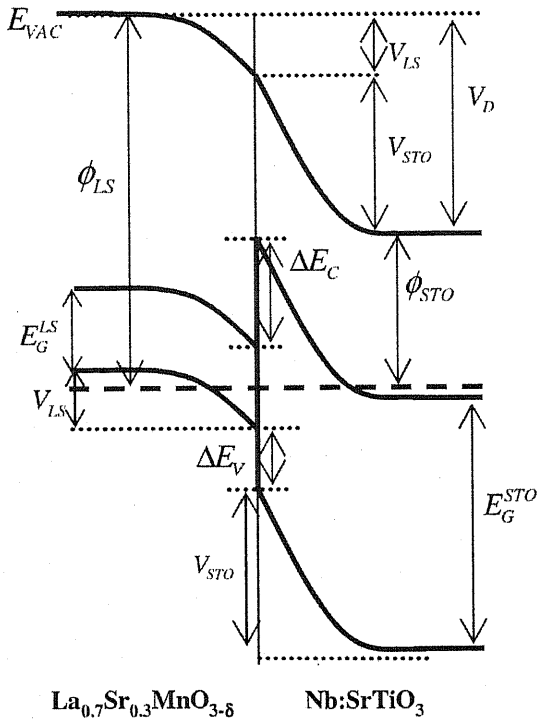

Figure 6.15: Interface band diagram showing the relevant energies according to the Anderson model [40].

and Nb:$SrTiO_3$. If we treat $La_{0.7}Sr_{0.3}MnO_{3-\delta}$ as a p-type semiconductor and the difference in the hole concentration as the only difference between $La_{0.7}Sr_{0.3}MnO_3$ and $La_{0.7}Sr_{0.3}MnO_{3-\delta}$, then this model predicts the built-in potential to be identical unless the work function of the manganites are different. In other words, the built-in potential is independent of doping. It is the *ratio* of the electrostatic potential at the interface between each semiconductor that is changing. In the present case, if hole concentration is reduced, the built-in potential decreases on the $La_{0.7}Sr_{0.3}MnO_{3(-\delta)}$ side and increases in the Nb:$SrTiO_3$ side, keeping the sum of the two constant. The band diagram is illustrated in Fig. 6.15 assuming a smaller band gap for $La_{0.7}Sr_{0.3}MnO_{3-\delta}$. The other extreme case of band alignment can be considered in analogy to the Bardeen model in metal-semiconductor interfaces. In this model, the band alignment is totally determined by the surface state density of the constituent semiconductors pinning the Fermi level [41]. The Fermi pinning effect results in an extra potential drop ζ_M at the interface when drawn relative to the vacuum level, giving a built-in potential of the form $V_{bi} = V_{STO} + V_{LS} - \zeta_M$. However, in order to consider the effect of doping on the built-in potential, detailed information on the surface state density is required.

Limiting our analysis to the Anderson model, the capacitance of the pn heterojunction is expressed as,

$$\begin{aligned} C &= \sqrt{\frac{qN_{eff}}{2(V_{bi}-V)}} \\ \frac{1}{N_{eff}} &= \frac{1}{\epsilon_{LS}N_{LS}} + \frac{1}{\epsilon_{STO}N_{STO}}. \end{aligned} \tag{6.3}$$

Here $\epsilon_{LS(STO)}$ and $N_{LS(STO)}$ are the dielectric permittivity and the doping concentration of $La_{0.7}Sr_{0.3}MnO_{3-\delta}$ (Nb:$SrTiO_3$). It is important to remember that here the capacitance is a function of the *product* of ϵ_{LS} and N_{LS}. If ϵ_{LS} is assumed to be independent of doping, Eq.(6.3) predicts a smaller capacitance for $La_{0.7}Sr_{0.3}MnO_{3-\delta}$ equivalent to an increase in C^{-2} which is opposite to what has been observed. Unlike the elemental metals, conductive oxide lattices are bonded mainly by ionic bonding which make them easily polarized [42] which can potentially increase ϵ_{LS}, although simultaneously the screening effect by the electrons should also be considered [43,44].

The above discussion indicates that application of the conventional semiconductor band alignment cannot explain the present results by simply assuming that hole concentration is the only relevant difference between $La_{0.7}Sr_{0.3}MnO_3$ and $La_{0.7}Sr_{0.3}MnO_{3-\delta}$. A systematic investigation of the C-V characteristics by varying the Sr concentration in $La_{1-x}Sr_xMnO_3$ should be carried out for further information.

IPE

The IPE spectra measured at 300 K normalized to the photoyield at 4.3 eV are shown in Fig. 6.16. Almost identical spectra are obtained for the two junctions with a slight difference in the low energy region. The barrier height deduced from the linear fitting shown in Fig. 6.16(b) are 1.18 V for $La_{0.7}Sr_{0.3}MnO_3$ and 1.31 V for $La_{0.7}Sr_{0.3}MnO_{3-\delta}$. The expected SBH from the Schottky-Mott relation is 0.7 $\pm$

0.1 eV using the work function value of data of 4.8±0.1 eV for $La_{0.7}Sr_{0.3}MnO_3$ [45] and the electron affinity of 4.1 eV for Nb:$SrTiO_3$ [46].

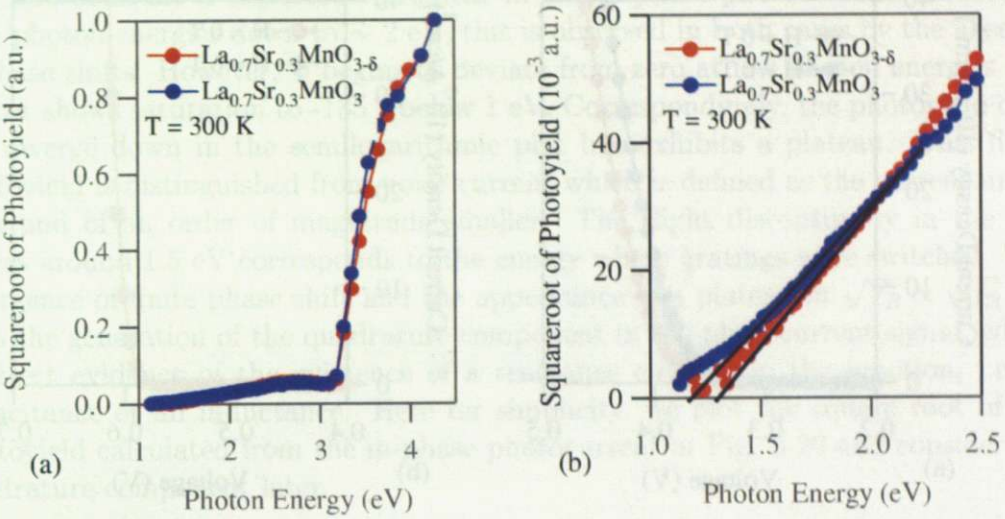

Figure 6.16: IPE spectra measured at 300 K for $La_{0.7}Sr_{0.3}MnO_{3(-\delta)}$/Nb:$SrTiO_3$. (a) Full spectra and the (b) magnified spectra for extracting the SBHs. The red (blue) line corresponds to $La_{0.7}Sr_{0.3}MnO_{3-\delta}$ ($La_{0.7}Sr_{0.3}MnO_3$).

6.4.3 Magnetic Field Dependent Junction Characterization

The magnetic field sensitivity in $La_{0.7}Sr_{0.3}MnO_{3(-\delta)}$/Nb:$SrTiO_3$ Schottky junctions were investigated at 10 K, where the magnetic field effect is most significant.

I-V Characteristics

The *I-V* characteristics of the two junctions under applied magnetic field at 10 K are displayed in Fig. 6.17. The difference in the magnetic response is clearly observed. The current increased under applied magnetic field in $La_{0.7}Sr_{0.3}MnO_{3-\delta}$ but not in $La_{0.7}Sr_{0.3}MnO_3$ consistent with the report by Nakagawa *et al.* [17]. In order to clarify the contribution of the bulk magnetization to the junction transport properties, *I-V* characteristics were also measured for $La_{0.7}Sr_{0.3}MnO_{3-\delta}$ with magnetic field applied parallel to the junction (Fig. 6.18). It is clear that there is no difference in the behavior between magnetic field parallel and perpendicular to the interface. This result strongly suggests that the bulk magnetization effect on the junction properties is negligibly small considering the large demagnetization factor in thin films.

IPE

Fig. 6.19 shows the IPE spectra taken at 10 K for $La_{0.7}Sr_{0.3}MnO_{3(-\delta)}$. On the left shown in red are the square root of the photoyields calculated from the magnitude of the photocurrents I_R ($= \sqrt{I_X^2 + I_Y^2}$). On the right axis, the phase shift

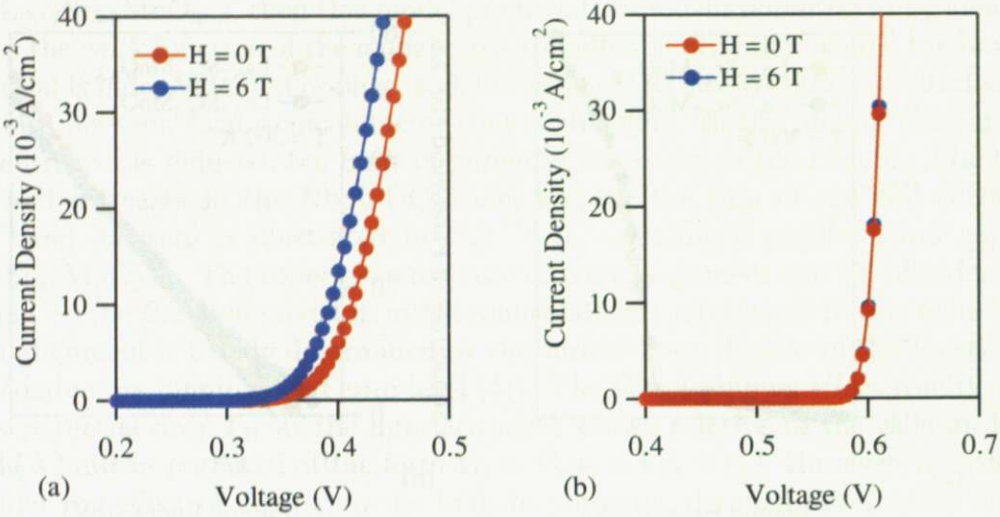

Figure 6.17: I-V characteristics of (a) $La_{0.7}Sr_{0.3}MnO_{3-\delta}$ and (b) $La_{0.7}Sr_{0.3}MnO_3$ junctions at T = 10 K under applied magnetic field of 0 T (red line) and 6 T (blue line).

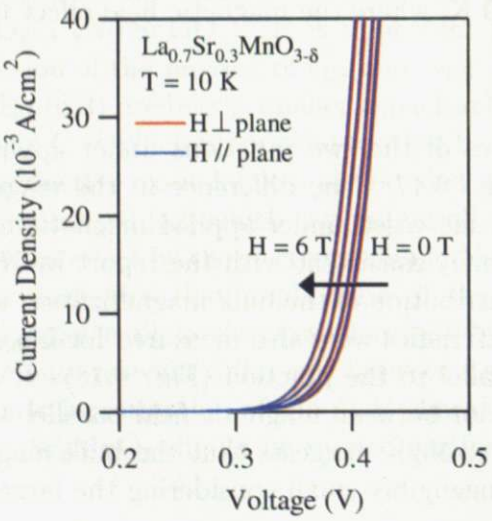

Figure 6.18: I-V characteristics of $La_{0.7}Sr_{0.3}MnO_{3-\delta}$ junctions at T = 10 K under applied magnetic field parallel (blue) and perpendicular (red) to the junction plane.

Φ ($= \tan^{-1}(I_Y/I_X)$) is depicted. Since the photoexcitation of the electrons is an instantaneous process compared with the frequency of the optical chopper, all the IPE photocurrent is expected to appear in the in-phase photocurrent. Indeed at high photon energies down to $\sim$ 2 eV, this is observed in both cases by the absence of phase shifts. However, Φ begins to deviate from zero at low photon energies and almost shows saturation to -135 ° below 1 eV. Correspondingly, the photoyield does not diverge down in the semilogarithmic plot but exhibits a plateau. This finite photoyield is distinguished from noise current which is defined as the current under dark and of an order of magnitude smaller. The slight discontinuity in the two curves around 1.5 eV corresponds to the energy where gratings were switched. The emergence of finite phase shift and the appearance of a plateau in $\sqrt{Y_R} \propto \sqrt{I_R}$ implies the generation of the quadrature component in the photocurrent signal, which is direct evidence of the existence of a reactance element in the junction, i.e. a capacitance or an inductance. Here for simplicity, we plot the square root of the photoyield calculated from the in-phase photocurrent in Fig. 6.20 and consider the quadrature component later.

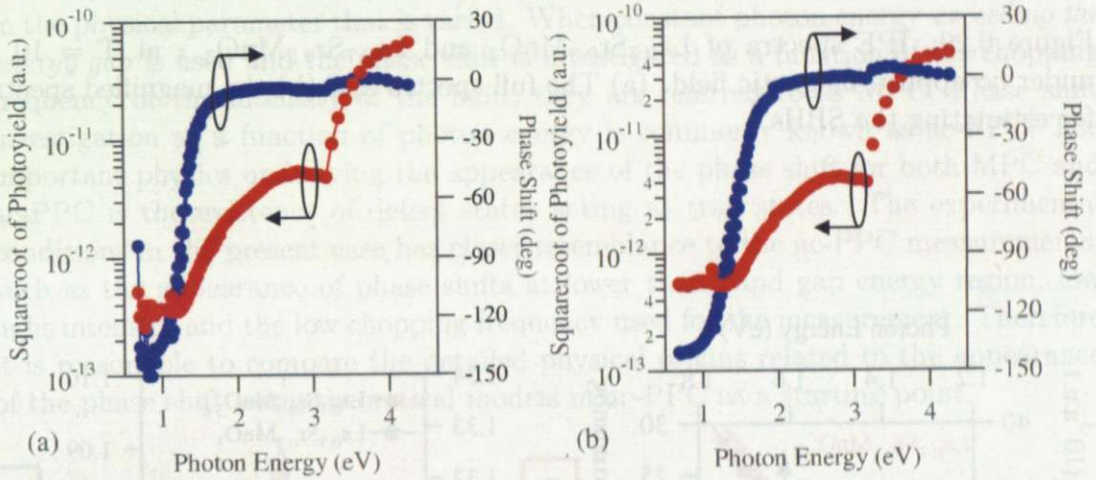

Figure 6.19: Square root of the photoyield from the magnitude of the photocurrent $\sqrt{Y_R}$ (red, left) and the phase shift of the photocurrent (blue, right) for (a)$La_{0.7}Sr_{0.3}MnO_{3-\delta}$ and (b)$La_{0.7}Sr_{0.3}MnO_3$ junctions.

The full spectra is shown in Fig. 6.20(a) where a rapid decrease in the photoyield above 3.2 eV corresponding to the electron-hole generation in Nb:$SrTiO_3$ and the gradual decrease below is observed. As seen in the magnified spectra in Fig. 6.20(b), both of these junctions present linear dependence on the square root of the photoyield, assuring the validity of the Fowler's relation. The IPE spectra measured under magnetic field of 6 T are shown in Fig. 6.21(a). There is a clear horizontal shift to lower photon energy in the IPE spectrum for $La_{0.7}Sr_{0.3}MnO_{3-\delta}$ whereas the spectrum of $La_{0.7}Sr_{0.3}MnO_3$ is independent of magnetic field. The parallel shift in the IPE spectrum is a strong implication of a shift in the SBH. The obtained SBH under different magnetic fields are summarized for $La_{0.7}Sr_{0.3}MnO_3$ and $La_{0.7}Sr_{0.3}MnO_{3-\delta}$ in Fig. 6.21(b). A systematic decrease in the SBH is seen

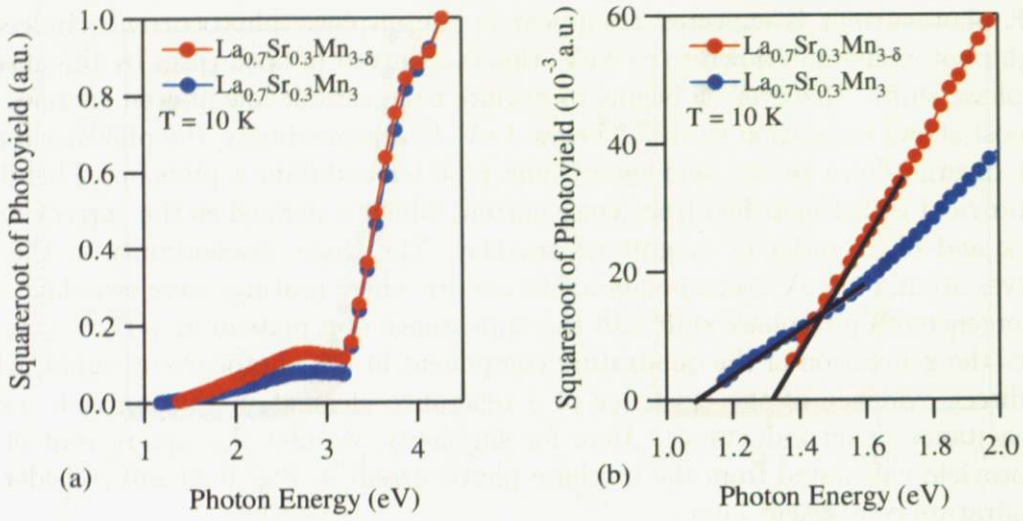

Figure 6.20: IPE spectra of $La_{0.7}Sr_{0.3}MnO_3$ and $La_{0.7}Sr_{0.3}MnO_{3-\delta}$ at T = 10 K under no applied magnetic field. (a) The full spectra and (b) the magnified spectra for estimating the SBHs.

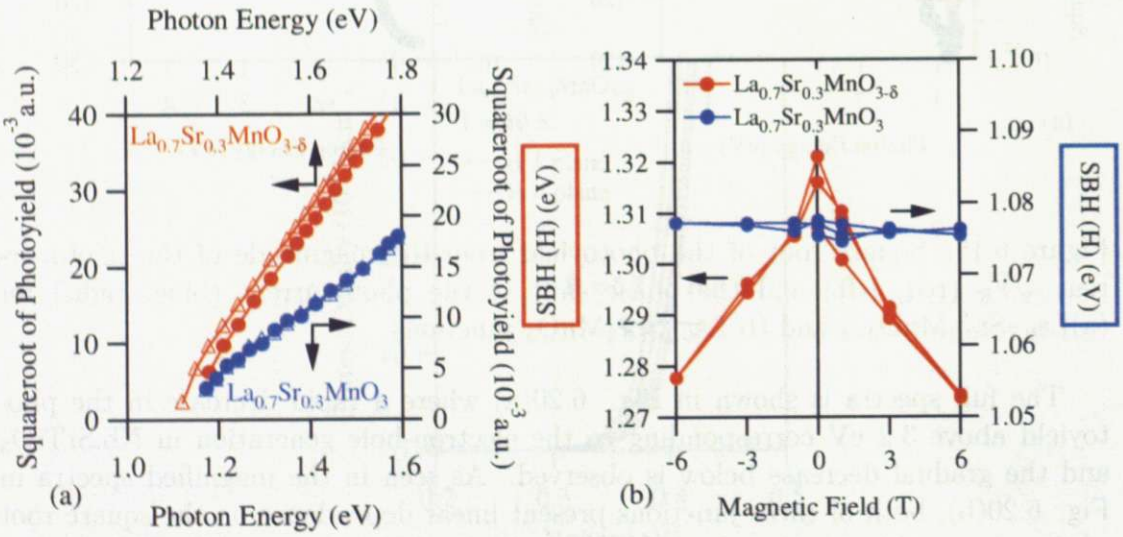

Figure 6.21: (a) IPE spectra from the in-phase photocurrent $\sqrt{Y_X}$ for $La_{0.7}Sr_{0.3}MnO_3$ (blue, right-bottom) and $La_{0.7}Sr_{0.3}MnO_{3-\delta}$ (red, left-top). (b) The obtained SBHs from (a).

for $La_{0.7}Sr_{0.3}MnO_{3-\delta}$ whereas it is independent of magnetic field for $La_{0.7}Sr_{0.3}MnO_3$. As has been discussed by Nakagawa *et al.*, [17] this change in SBH is opposite in direction and of much larger magnitude to what is expected from a simple Zeeman splitting [47, 48].

Quadrature Component

The appearance of phase shifts in $La_{0.7}Sr_{0.3}MnO_{3(-\delta)}$/Nb:$SrTiO_3$ junctions at low photon energies is suggestive of the presence of a reactance element in the device. Since the quadrature component evolves with the illuminated photon energy, the reactance element in question is also a photosensitive element.

Analogous phase shift of the photocurrent under chopped light illumination has been reported under the names of modulated photoconductivity (MPC) [49] and ac-primary photocurrent measurements (ac-PPC) [50] in amorphous semiconductors. A schematic diagram of the measurement system is illustrated in Fig. 6.22(a) which is the same for both techniques. The ac-photocurrent is recorded as the frequency, light intensity or the photon energy is varied. The difference between the two techniques is in the physical parameter that is varied. When constant photon energy *exceeding the energy gap* is used and the phase shift is investigated as a function of the chopping frequency or the intensity of the light, they are referred to as MPC. Phase shift investigation as a function of photon energy is commonly known as ac-PPC. The important physics underlying the appearance of the phase shift for both MPC and ac-PPC is the existence of defect states acting as trap states. The experimental conditions in the present case has closer resemblance to the ac-PPC measurements, such as the appearance of phase shifts at lower than band gap energy region, low light intensity and the low chopping frequency used for the measurement. Therefore it is reasonable to compare the detailed physical origins related to the appearance of the phase shift using theoretical models in ac-PPC as a starting point.

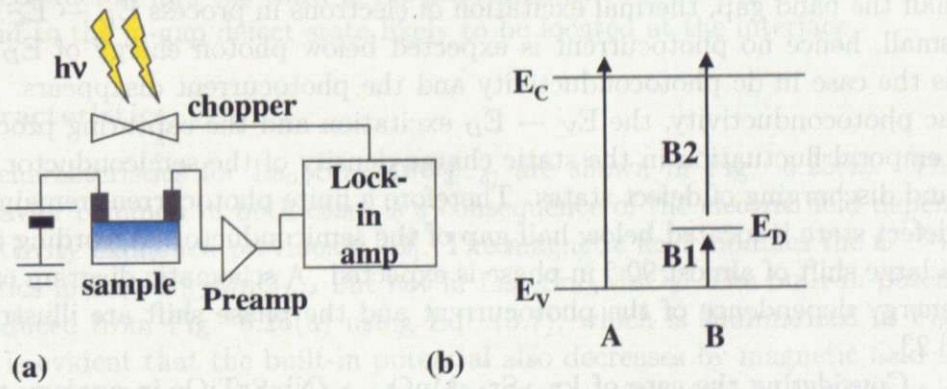

Figure 6.22: (a) Schematic diagram of the experimental setup in MPC or ac-PPC. (b) Energy diagram showing the relevant energy levels for ac-PPC and the corresponding transitions.

The energy band diagram for the relevant processes are depicted in Fig. 6.22(b). The localized defect states within the band-gap E_D can act as a trapping state

which leads to two-step excitation by combination of photoexcitation and thermal excitation depending on the photon energy.

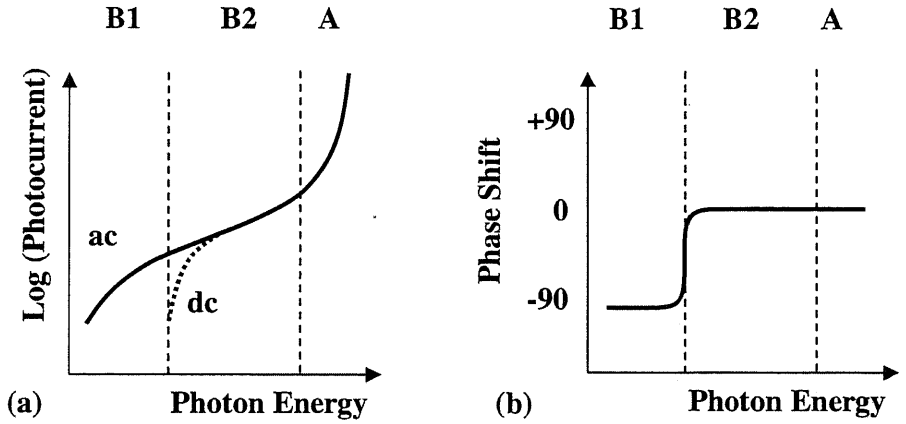

Figure 6.23: Schematic diagram of the photon energy dependence in the (a) photocurrent in logarithmic scale and (b) the phase shift in ac- and dc- PPC.

By modeling these processes in a three level system under ac illumination of light, Okamoto has derived formulae relating the occupation of the defect states and the chopping frequency [50]. The theoretical derivation concludes that a phase shift in the photocurrent appears as the excitation process changes from direct photoexcitation (process A) to thermal + B2 to B1 + thermal. In process A no phase shift is expected because the process is independent of the defect states. Depending on the relative energy level of the defect state, a phase shift is expected at the photon energy coincident with the corresponding energy gap, namely E_C-E_D for process B2 and E_D - E_V for process B1. It is natural to expect that when E_D is located below half the band gap, thermal excitation of electrons in process $E_D \rightarrow E_C$ is extremely small, hence no photocurrent is expected below photon energy of E_D - E_V. This is the case in dc photoconductivity and the photocurrent disappears. However, in ac photoconductivity, the $E_V \rightarrow E_D$ excitation and the capturing process causes a temporal fluctuation in the static charge density of the semiconductor by charging and discharging of defect states. Therefore a finite photocurrent remains even if the defect state is located below half gap of the semiconductor. According to Okamoto, a large shift of almost 90 ° in phase is expected. A schematic diagram of the photon energy dependence of the photocurrent and the phase shift are illustrated in Fig. 6.23.

Considering the case of $La_{0.7}Sr_{0.3}MnO_{3(-\delta)}$/Nb:$SrTiO_3$ in analogy to the above ac-PPC model, the equivalent of the dangling bond states in a:Si-H could be some defect states in the vicinity of the interface on the Nb:$SrTiO_3$ side or on the $La_{0.7}Sr_{0.3}MnO_{3(-\delta)}$ side. The presence of the behavior in both junctions suggests that the defect states are more likely to be located on the Nb:$SrTiO_3$ side. However, the magnetic field dependence of the phase shift shown in Fig. 6.24 reveals that the phase shift is also magnetic field sensitive, for which the change in the magnitude is inexplicable by the shift in I_X. Therefore it is likely that the defect states are

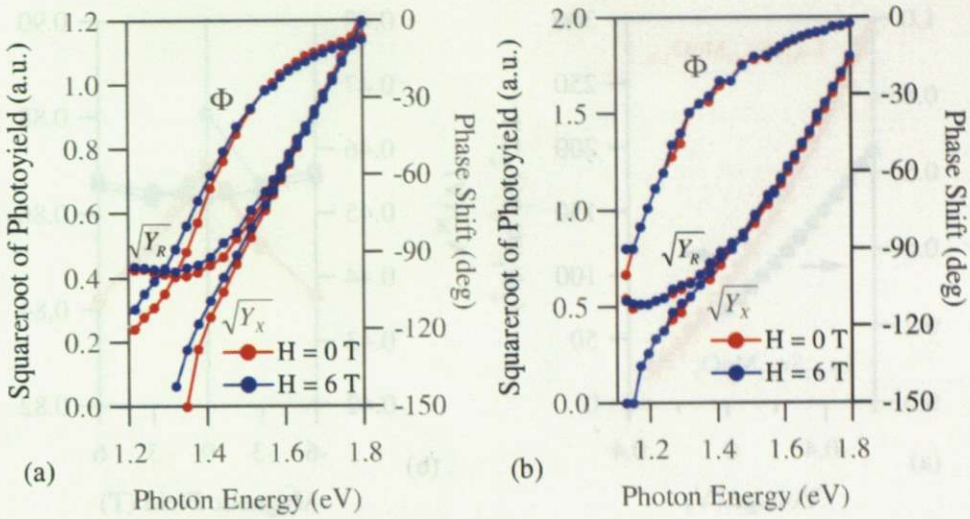

Figure 6.24: $\sqrt{Y_R}$ and $\sqrt{Y_X}$ (left) and Φ (right) measured under applied magnetic filed in (a)$La_{0.7}Sr_{0.3}MnO_{3-\delta}$ and (b)$La_{0.7}Sr_{0.3}MnO_3$.

located at the interface and consists of the nature of both $La_{0.7}Sr_{0.3}MnO_{3(-\delta)}$ and Nb:$SrTiO_3$. Typical examples of defects in perovskite oxides include point defects such as oxygen and cation vacancies, dislocations due to lattice mismatch, local segregation of secondary phase formation [51]. For further clarification of the origin of the phase shift, we believe that a systematic study in the fabrication condition dependence is required.

In conclusion, the IPE spectra obtained at low temperature is a sum three transport processes. First is the electron-hole generation in the semiconductor above the band gap, second is the photocurrent from the photoexcited electrons in the metal to the semiconductor, and the third is the photoexcitation from the semiconductor valence band to the in-gap defect state likely to be located at the interface.

C-V Characteristics

The *C-V* characteristics for $La_{0.7}Sr_{0.3}MnO_{3(-\delta)}$ are shown in Fig. 6.25(a). The curved behavior common in both cases is a consequence of the electric field dependent permittivity explained previously [52]. The magnetic field modifies the C^{-2}-V characteristics in $La_{0.7}Sr_{0.3}MnO_{3-\delta}$ but not in $La_{0.7}Sr_{0.3}MnO_3$. The built-in potential was deduced from Fig. 6.25(a) using Eq. (5.7), which is summarized in Fig. 6.25(b). It is evident that the built-in potential also decreases by magnetic field in the case of $La_{0.7}Sr_{0.3}MnO_{3-\delta}$ but not for $La_{0.7}Sr_{0.3}MnO_3$. If the ratio of the change in the built-in potential and the SBH obtained from IPE are compared (Fig. 6.26(a)), the change in the ratio of each value agrees very well. However, when the magnitude of the values are compared (Fig. 6.26(b)), there is a difference almost by a factor of two. This difference cannot be ascribed to the correction term ξ from the energy difference between the conduction band bottom and the Fermi level. It is intriguing that a similar oxide metal $SrRuO_3$/Nb:$SrTiO_3$ does not show this discrepancy but

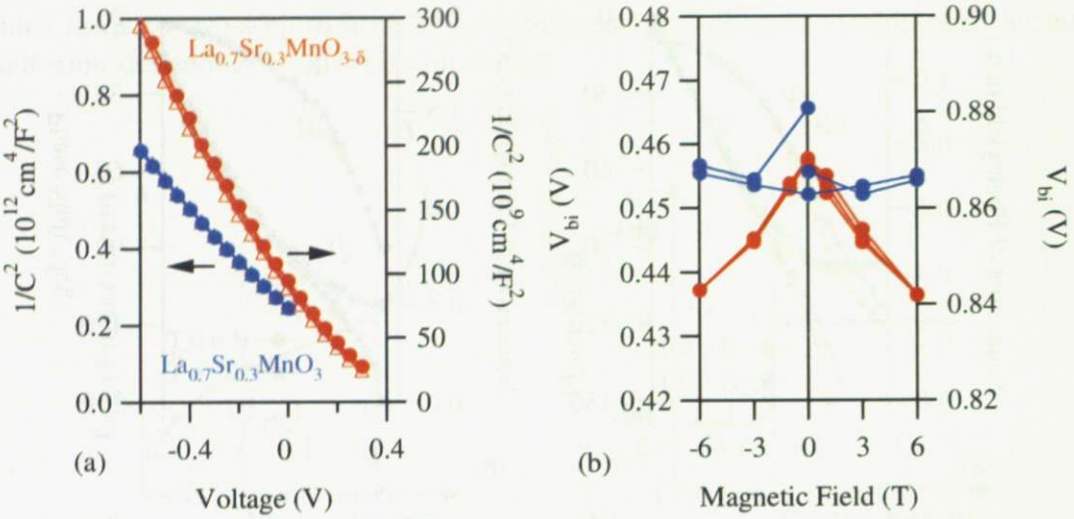

Figure 6.25: (a) $1/C^2$ vs. V for $La_{0.7}Sr_{0.3}MnO_3$ (blue, left) and $La_{0.7}Sr_{0.3}MnO_{3-\delta}$ (red, right) at 10 K. (b) Obtained built-in potential against applied magnetic field for $La_{0.7}Sr_{0.3}MnO_3$ (blue, left) and $La_{0.7}Sr_{0.3}MnO_{3-\delta}$ (red, right).

$La_{0.7}Sr_{0.3}MnO_{3(-\delta)}$ does. Two possibilities for the discrepancy are considered below.

One possibility is the existence of an additional parallel capacitance in the device, reducing the built-in potential obtained from the C^{-2} versus V plot as shown in Fig. 6.27. An obvious candidate for the parallel capacitance would be trap states inside Nb:$SrTiO_3$, which is consistent with the discussion on the phase shift at low photon energy in IPE. However the fact that the discrepancy between C-V and IPE is absent in $SrRuO_3$ suggests that if present, the trap states are more likely to be in the $La_{0.7}Sr_{0.3}MnO_{3(-\delta)}$ side.

Another possibility is the existence of an interface dipole at the interface. If a dipole is present at the interface, an electrostatic potential is created at the interface causing different barrier heights on each side of the interface. Since the two probes involved independently measures the barrier height on each side, it can be expected that the two SBHs are different for each measurement. Related result supporting the non-idealistic barrier height formation in $La_{0.7}Sr_{0.3}MnO_3$ has been reported using photoemission spectroscopy in the same structure by Minohara *et al.* [53] shown in Fig. 6.28. Whilst $SrRuO_3$/Nb:$SrTiO_3$ Schottky barrier is consistent with the Schottky-Mott relation, the $La_{0.7}Sr_{0.3}MnO_3$/Nb:$SrTiO_3$ Schottky barrier height deviates from this relationship implying the importance of the microscopic origins in the formation of SBH.

6.4.4 Possible Origins of $\Phi_{SB}(H)$

The origin of the reduction of the SBH by magnetic field in $La_{0.7}Sr_{0.3}MnO_{3-\delta}$ is considered from the following three different perspectives.

1. Schottky-Mott model

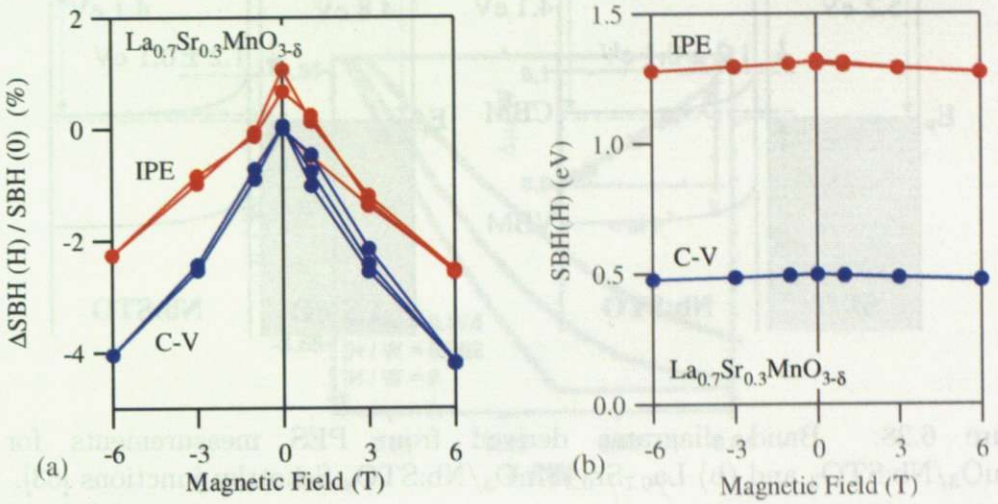

Figure 6.26: (a) Relative change in the built-in potential from C-V (Φ_{SB}^{C-V}) and SBH from IPE (Φ_{SB}^{IPE}) and (b) the absolute values of Φ_{SB}^{C-V} an by applied magnetic field.

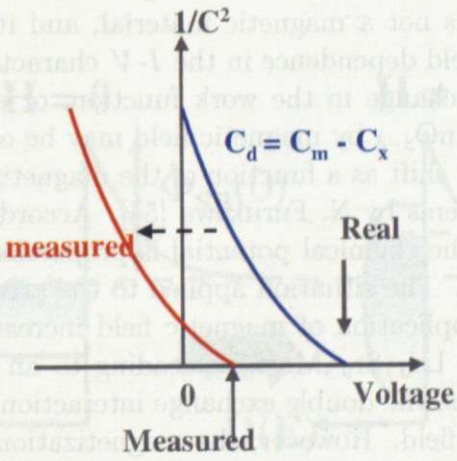

Figure 6.27: Illustration of the apparent $1/C^2$-V behavior (red) being shifted to lower voltage from the real capacitance (blue) due to the additional parallel capacitance present in the device.

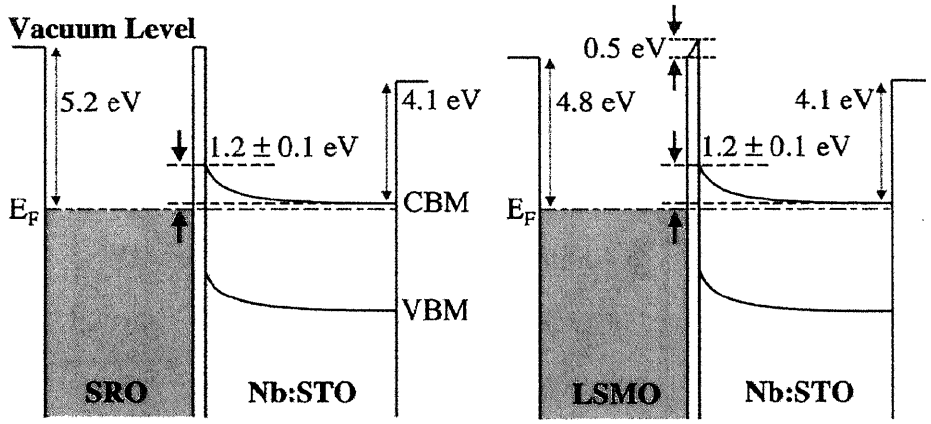

Figure 6.28: Band diagrams derived from PES measurements for (a) $SrRuO_3$/Nb:STO_3 and (b) $La_{0.7}Sr_{0.3}MnO_3$/Nb:STO_3 Schottky junctions [53].

2. Interface dipole model

3. Interface charge transfer model

Schottky-Mott Model

From the simplest understanding of Schottky barrier formation, the SBH is determined by the work function of the metal and the electron affinity of the semiconductor. A change in SBH by magnetic field implies a change in either of the two physical quantities. It is natural to believe that the magnetic field dependence is not arising from Nb:$SrTiO_3$ for it is not a magnetic material, and it is confirmed by the absence of the magnetic field dependence in the I-V characteristics of Au/Nb:$SrTiO_3$ junctions. Therefore a change in the work function, or equivalently the chemical potential, of $La_{0.7}Sr_{0.3}MnO_{3-\delta}$ by magnetic field may be occurring.

A chemical potential shift as a function of the magnetization has been proposed in double exchange systems by N. Furukawa [54]. According to this scenario, at a constant temperature, the chemical potential is proportional to $< M^2 >$ as shown in the inset of Fig. 6.29. The situation applied to the present case is schematically drawn in Fig. 6.30. Application of magnetic field increases $< M^2 >$, broadening the conduction band in $La_{0.7}Sr_{0.3}MnO_{3-\delta}$, leading to an increase in the chemical potential. In other words, the double exchange interaction enhances the bandwidth with stronger magnetic field. However, the magnetization at 10 K is almost saturated in both junctions, which questions the magnitude of the effect. More importantly, the appearance of the magnetic field dependence only in $La_{0.7}Sr_{0.3}MnO_{3-\delta}$ requires a drastic difference in the density of states between $La_{0.7}Sr_{0.3}MnO_3$ and $La_{0.7}Sr_{0.3}MnO_{3-\delta}$ for this effect to be present. Therefore we conclude that the chemical potential shift is not the dominating origin of the magnetic field dependence of SBH in $La_{0.7}Sr_{0.3}MnO_{3-\delta}$.

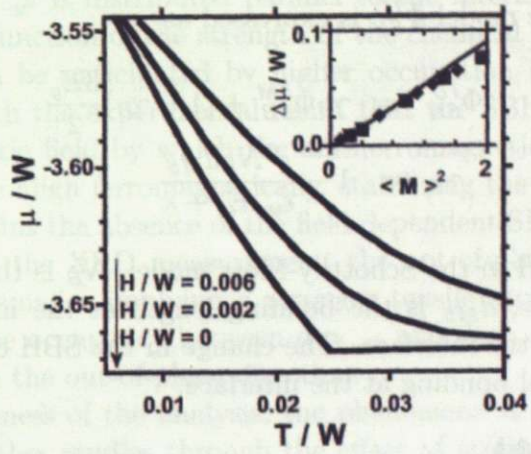

Figure 6.29: Temperature dependence of μ at different magnetic fields. Inset:$\Delta\mu/W$ as a function of $< M^2 >$. Lines show the case for $H = 0$ and Squares and diamonds are data at $T = 1.01T_C$ and $T = 1.2T_C$, respectively.

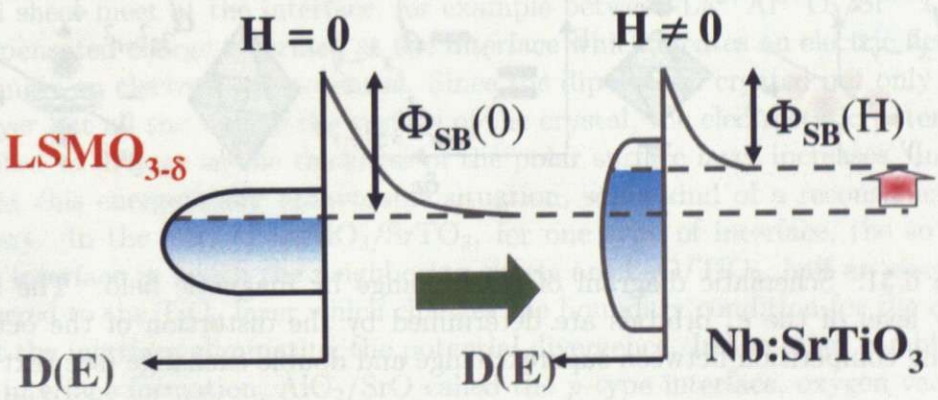

Figure 6.30: Schematic diagram illustrating the chemical potential shift by application of magnetic field in $La_{0.7}Sr_{0.3}MnO_{3-\delta}$.

Interface Dipole

In addition to the work functions in the bulk on both sides, the interface chemical bonds also contribute to the formation of Schottky barrier heights [55]. The SBH in the interface dipole model Φ_{SB}^{ID} is expressed as

$$\begin{aligned} \Phi_{SB}^{ID} &= \gamma_B \Phi_{SB}^{SM} + (1-\gamma_B)\frac{3E_g}{2} \\ \gamma_B &= 1 - \frac{q^2 N_B d_{MS}}{\epsilon_{int} E_g + \kappa} \end{aligned} \tag{6.4}$$

where Φ_{SB}^{SM} is the SBH in the Schottky-Mott model, N_B is the number of chemical bonds at the interface, d_{MS} is the bonding length at the interface and ϵ_{it} is the dielectric constant at the interface. The change in the SBH can be induced by the change in the chemical bonding at the interface.

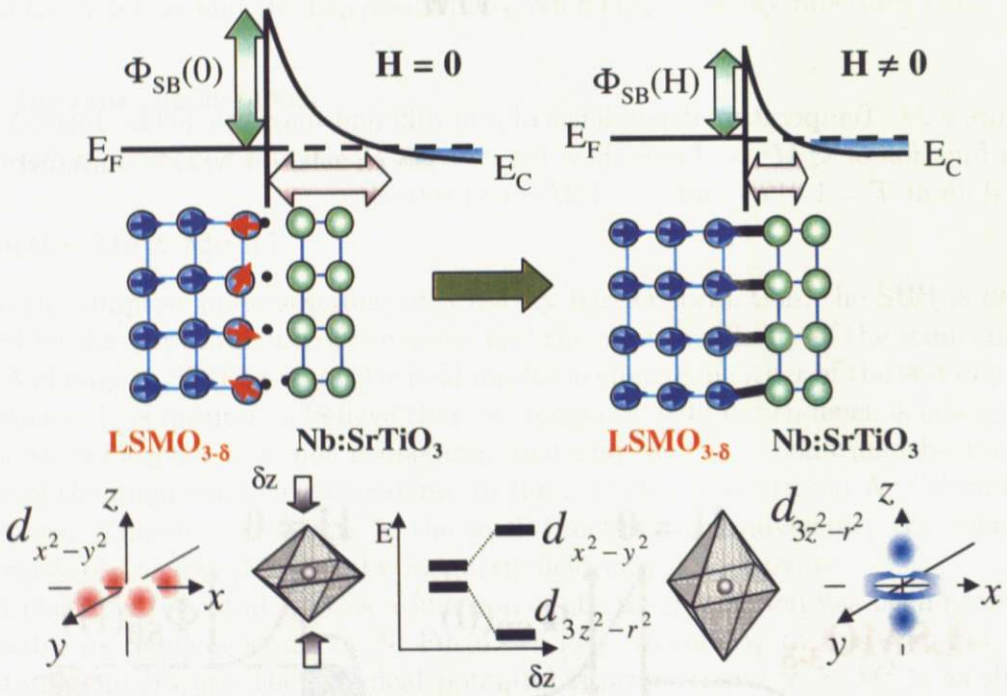

Figure 6.31: Schematic diagram of SBH change by magnetic field. The relative energy level of the e_g orbitals are determined by the distortion of the octahedra inducing competition between superexchange and double exchange (see text for detail).

Through the investigation of electronic and magnetic structures at the surface or interfaces in manganite [56–58], it has been discussed that the breaking of the symmetry induces a change in the electrostatic potential modifying the relative energy scale of the occupied e_g orbitals on Mn ions [59, 60]. This difference in the occupancy induces a competition between double exchange and superexchange. In many cases, it has been speculated that the antiferromagnetic state is more

stable because of the lower $d_{x^2-y^2}$ energy compared with $d_{3z^2-r^2}$. This can cause serious effects on the chemical bonds at the interface because of the difference in the spatial distribution of the two orbitals. $d_{3z^2-r^2}$ orbitals are oriented towards the interface whereas $d_{x^2-y^2}$ is distributed parallel to the interface. Since the second term in Eq. 6.4 is a function of the strength of the chemical bond at the interface, the enhancement can be anticipated by higher occupation in the $d_{3z^2-r^2}$ orbital. This is consistent with the experimental result that the SBH is decreasing by the application of magnetic field by which the antifierromagnetically aligned interface t_{2g} spins are forced to align ferromagnetically, stabilizing the ferromagnetic ground state. This also explains the absence of the field dependent SBH in $La_{0.7}Sr_{0.3}MnO_3$. As can be seen from the XRD measurement, the out-of-plane lattice constant of $La_{0.7}Sr_{0.3}MnO_{3-\delta}$ is smaller implying a stronger tensile strain, which accelerates the competition of the occupancy between $d_{3z^2-r^2}$ and $d_{x^2-y^2}$ because of the larger Coulomb repulsion in the out-of-plane direction.

Despite the crudeness of the analysis, the phenomena is consistently explained in this scenario. Further studies through the effect of strain should be decisive in confirming the validity of this scenario.

Interface Charge Transfer

The previous two perspectives have been direct applications of the established concepts mainly in conventional semiconductors. The perspective of charge transfer at perovskite interfaces is a concept recently drawing much attention [61, 62].

When a perovskite structure is viewed from the [010] or [100] direction, the stacking can be seen as a sequence of $\cdots$ - AO - BO_2 - AO - $\cdots$ planes. Depending on the valence of the B-site cation, the sheet charge density on each plane is $\cdots$ - +1 - -1 - +1 - $\cdots$ in case of $A^{3+}B^{3+}O_3$, or $\cdots$ - 0 - 0 - 0 - $\cdots$ in the case of $A^{2+}B^{4+}O_3$, where each layer is charge neutral. When a perovskite with charged sheets and charge neutral sheet meet at the interface, for example between $La^{3+}Al^{3+}O_3/Sr^{2+}Ti^{4+}O_3$, uncompensated charge is formed at the interface which creates an electric field and accordingly an electrostatic potential. Since the dipoles are created not only in the first layer but all the way to the surface of the crystal, the electrostatic potential is calculated to diverge as the thickness of the polar surface layer increases. In order to avoid this energetically unfavorable situation, some kind of a reconstruction is necessary. In the case of $LaAlO_3/SrTO_3$, for one type of interface, the so called n-type interface in which the neighboring sheets are LaO/TiO_2, half an electron is transferred to the TiO_2 layer which changes the boundary condition for the electric field at the interface eliminating the potential divergence. In the other combination of the interface formation, AlO_2/SrO called the p-type interface, oxygen vacancies are introduced to avoid the potential divergence because there is no valence degree of freedom in Al.

A similar situation can be imagined in the case of $La_{0.7}Sr_{0.3}MnO_{3(-\delta)}/SrTiO_3(001)$ (Fig. 6.32(a)). $La_{0.7}Sr_{0.3}MnO_{3(-\delta)}$ is classified as a polar stacking sequence when viewed along the [001] direction; therefore, when an interface is formed with $SrTiO_3$, a reconstruction is necessary to avoid the potential divergence. The present case of $La_{0.7}Sr_{0.3}MnO_{3(-\delta)}$ differs from that of $LaAlO_3/SrTO_3$ in that Mn can access the va-

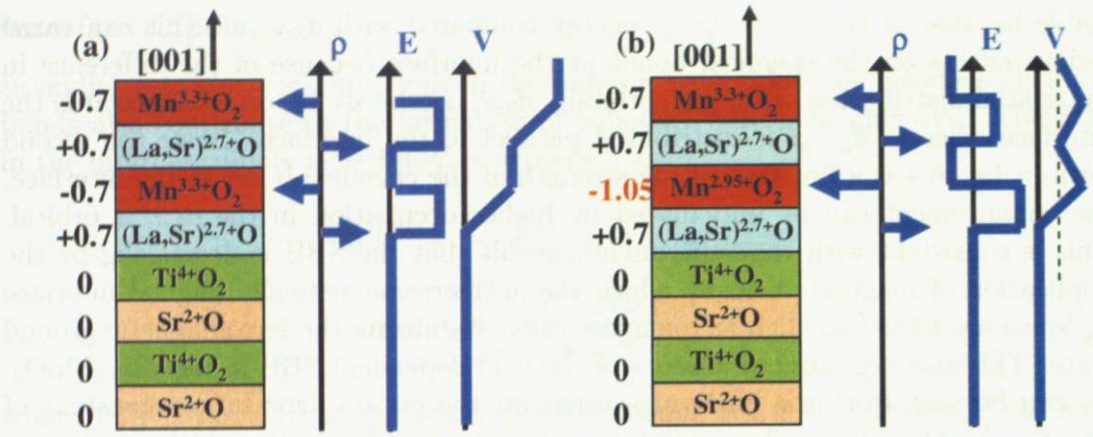

Figure 6.32: Schematic diagram of the stacking of $La_{0.7}Sr_{0.3}MnO_3$ / Nb:$SrTiO_3$ in the [001] direction presenting the dipoles, electric field and the electrostatic potential generated by the polar discontinuity at the interface (a) without electronic reconstruction and (b) after reconstruction by charge transfer of electron into MnO_2 layer.

lence of both Mn^{2+} or Mn^{4+}, enabling the change in the valence state for the change in the boundary conditions (Fig. 6.32(b)). If electrons are doped at the interface on the $La_{0.7}Sr_{0.3}MnO_{3(-\delta)}$ side, the $La_{0.7}Sr_{0.3}MnO_{3(-\delta)}$ layer closest to the interface has a lower hole concentration compared with the rest of the thin film. Therefore the situation at the interface can be illustrated as shown in Fig. 6.33(a). In the case of $La_{0.7}Sr_{0.3}MnO_3$, the difference in the hole concentration does not change the ground state because the hole concentration is far away from the concentration for inducing a metal-insulator transition as can be seen with reference to Fig. 6.8. On the other hand, for $La_{0.7}Sr_{0.3}MnO_{3-\delta}$, the reduced hole concentration is close to or crossing this critical concentration. By application of magnetic field, a small difference is expected for $La_{0.7}Sr_{0.3}MnO_3$ but for $La_{0.7}Sr_{0.3}MnO_{3-\delta}$, the magnetic field may cross the critical concentration forcing the interface to order in the ferromagnetic metallic phase.

A decisive measurement would be to fabricate a stoichiometric $La_{1-x}Sr_xMnO_3$ /Nb:$SrTiO_3$ junction and measure IPE under applied magnetic field. The result is shown in Fig. 6.34(b) together with the magnetoresistance of $La_{1-x}Sr_xMnO_3$ /$SrTiO_3$(001). As can be seen from the magnetoresistance Fig. 6.34(a), the film shows an insulating behavior with a reduced T_C of $\sim$ 200 K. As the magnetic field is increased, a systematic increase in the slope of the IPE spectra is observed. However the linearly extrapolated photon energy remains the same implying that the SBH is magnetic field independent. This fact suggests us that the magnetic field sensitivity in $La_{0.7}Sr_{0.3}MnO_{3-\delta}$ does not arise simply from the reduction in the hole concentration.

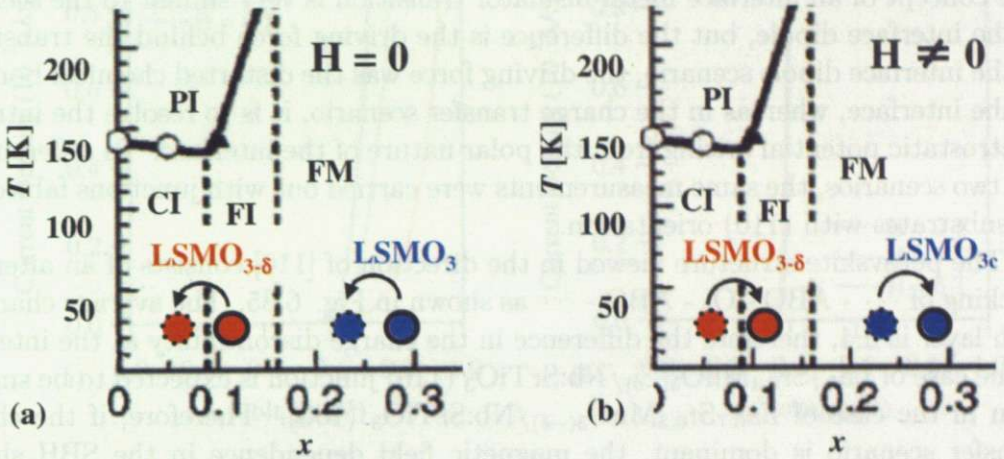

Figure 6.33: Part of the phase diagram [37] illustrating the interface magnetic/electronic structure for $La_{0.7}Sr_{0.3}MnO_{3(-\delta)}$ (a) under no magnetic field and (b) under applied magnetic field. The reduced hole concentration at the interface by charge transfer is depicted by arrows.

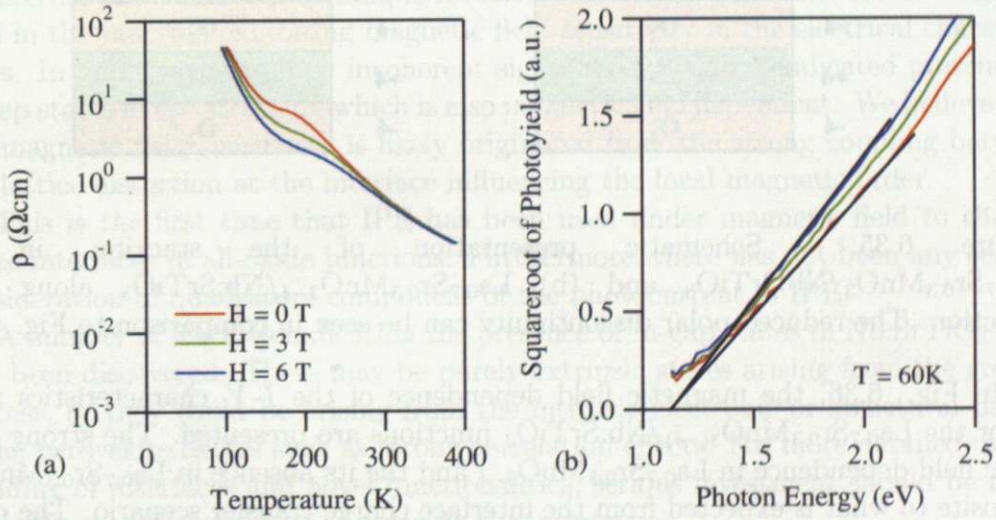

Figure 6.34: (a) Temperature dependent resistivity under applied magnetic field in $La_{1-x}Sr_xMnO_3$ (x = 0.10)/$SrTiO_3$(001) and (b) IPE spectra measured under applied magnetic field at 60 K for $La_{1-x}Sr_xMnO_3$ (x = 0.10) / Nb:$SrTiO_3$(001).

Junctions on Nb:$SrTiO_3$(110) Substrates

The concept of an interface metal-insulator transition is very similar to the scenario of the interface dipole, but the difference is the driving force behind the transition. In the interface dipole scenario, the driving force was the distorted chemical bonding at the interface, whereas in the charge transfer scenario, it is to resolve the intrinsic electrostatic potential arising from the polar nature of the interface. To differentiate the two scenarios, the same measurements were carried out with junctions fabricated on substrates with (110) orientation.

The perovskite structure viewed in the direction of [110] consists of an alternate stacking of $\cdots$ - ABO - O_2 - ABO - $\cdots$ as shown in Fig. 6.35. The average charge in each layer is ± 4, therefore the difference in the charge discontinuity at the interface in the case of $La_{0.7}Sr_{0.3}MnO_{3(-\delta)}$/Nb:$SrTiO_3$ (110) junction is expected to be smaller than in the case of $La_{0.7}Sr_{0.3}MnO_{3(-\delta)}$/Nb:$SrTiO_3$ (100). Therefore, if the charge transfer scenario is dominant, the magnetic field dependence in the SBH should diminish in the case of (110) junction.

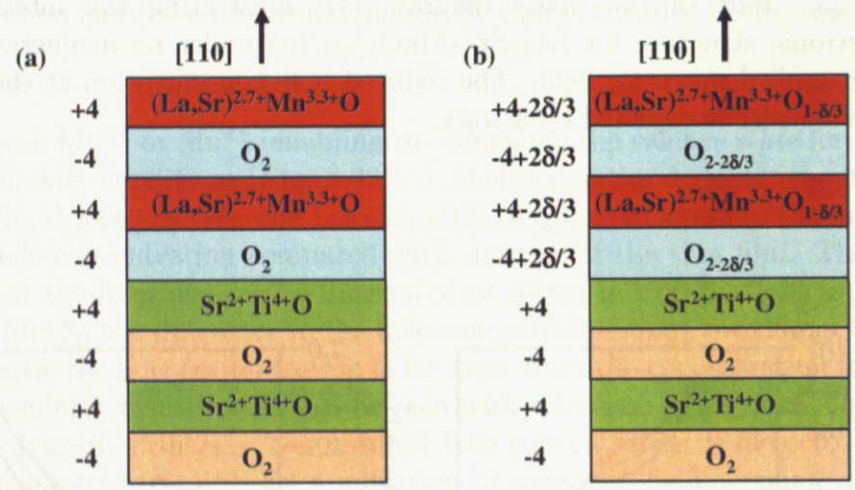

Figure 6.35: Schematic presentation of the stacking in (a) $La_{0.7}Sr_{0.3}MnO_3$/Nb:$SrTiO_3$ and (b) $La_{0.7}Sr_{0.3}MnO_{3-\delta}$/Nb:$SrTiO_3$ along [110] direction. The reduced polar discontinuity can be seen in comparison to Fig. 6.32.

In Fig. 6.36, the magnetic field dependence of the I-V characteristics at 10 K for the $La_{0.7}Sr_{0.3}MnO_{3(-\delta)}$/Nb:$SrTiO_3$ junctions are presented. The strong magnetic field dependence in $La_{0.7}Sr_{0.3}MnO_{3-\delta}$ and the its absence in $La_{0.7}Sr_{0.3}MnO_3$ is opposite to what is expected from the interface charge transfer scenario. The quantitative differences are likely to have been the results of the subtle growth condition differences.

Therefore, out of the scenarios we have considered, we believe that the magnetic field dependence in the SBH is more likely a consequence of the interface lattice distortion modifying the local chemical bonds at the interface.

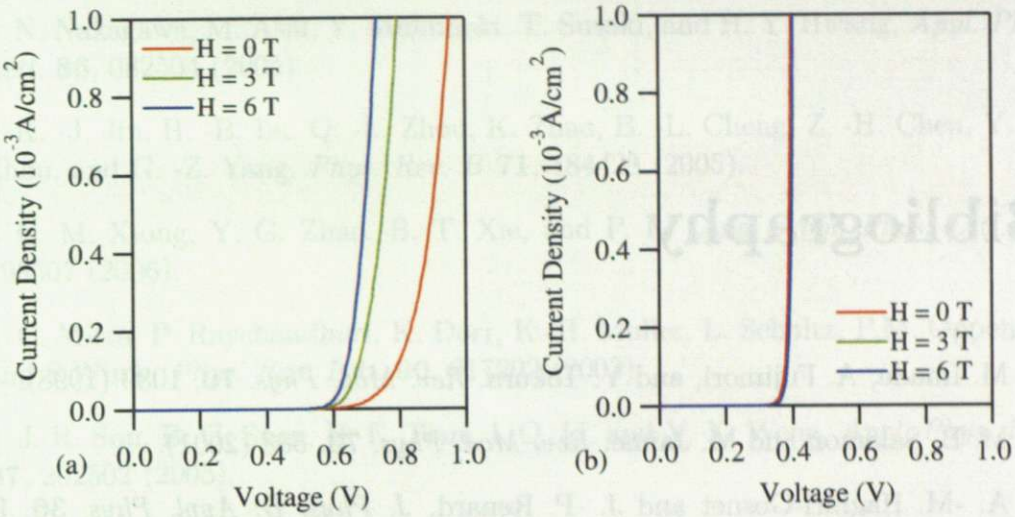

Figure 6.36: I-V characteristics under applied magnetic field at 10 K for (a)$La_{0.7}Sr_{0.3}MnO_{3-\delta}$ and (b) $La_{0.7}Sr_{0.3}MnO_3$ grown on Nb:$SrTiO_3$ (110) substrate. The strong magnetic field dependence in $La_{0.7}Sr_{0.3}MnO_{3-\delta}$ disfavors the SBH reduction driven by a charge transfer scenario.

6.5 Conclusions

We have investigated the effect of magnetic order at the interface of an oxide Schottky junction in $La_{0.7}Sr_{0.3}MnO_{3(-\delta)}$ /Nb:$SrTiO_3$. Direct characterization of the SBH by internal photoemission technique revealed a decrease in the SBH under magnetic field in the junction exhibiting magnetic field sensitivity in the electrical characteristics. In addition, the phase incoherent signal from IPE has indicated presence of in-gap states in the structure which is also magnetic field dependent. We believe that the magnetic field sensitivity is likely originated from the strong coupling between the lattice distortion at the interface influencing the local magnetic order.

This is the first time that IPE has been used under magnetic field to characterize interfaces in all-oxide junctions. Furthermore, there has not been any serious consideration of quadrature component of the photocurrent in IPE.

A number of features indicating the presence of in-gap states in Nb:$SrTiO_3$ have also been discovered. These may be purely extrinsic states arising from the growth process, or they could be arising from the intrinsic electronic or structural nature of the perovskite oxides such as strong correlation effects. For more detailed understanding of interfaces and novel functionalities, serious investment should be made to clarify these in-gap states hidden at the interfaces.

Bibliography

[1] M. Imada, A. Fujimori, and Y. Tokura, *Rev. Mod. Phys.* **70**, 1039 (1998).

[2] M. B. Salamon and M. Jaime, *Rev. Mod. Phys.* **73**, 583 (2001).

[3] A. -M. Haghiri-Gosnet and J. -P. Renard, *J. Phys. D: Appl. Phys.* **36**, R127 (2003).

[4] K. Dorr, *J. Phys. D: Appl. Phys.* **39**, R125 (2006).

[5] P. -G. DeGennes, *Phys. Rev.* **118**, 141 (1960).

[6] P. W. Anderson and H. Hasegawa, *Phys. Rev.* **100**, 675 (1961).

[7] J. Kanamori, *J. Appl. Phys.* **31**, S145 (1960).

[8] Y. Tokura, A. Urushibara, Y. Moritomo, T. Arima, A. Asamitsu, G. Kido, and N. Furukawa, *J. Phys. Soc. Japan* **63**, 3931 (1994).

[9] P. Schiffer, A. P. Ramirez, W. Bao, and S. -W. Cheong, *Phys. Rev. Lett.* **75**, 3336 (1995).

[10] Y. Tokura, Y. Tomioka, Y. Kuwahara, A. Asamitsu, Y. Moritomo, and M. Kasai, *J. Appl. Phys.* **79**, 5288 (1996).

[11] M. McCormack, S. Jin, T. H. Tiefel, R. M. Flemming, J. M. Philips, and R. Ramesh, *Appl. Phys. Lett.* **64**, 3045 (1994).

[12] Y. Lu, X. W. Li, G. Q. Gong, G. Xiao, A. Gupta, P. Lecoeur, J. Z. Sun, Y. Y. Wang, and V. P. Dravid, *Phys. Rev. B* **54**, R8357 (1996).

[13] J. Z. Sun, W. J. Gallagher, P. R. Duncombe, L. Krusin-Elbaum, R. A. Altman, A. Gupta, Y. Lu, G. Q. Gong, and G. Xiao, *Appl. Phys. Lett.* **69**, 3266 (1996).

[14] Y. Ogimoto, M. Izumi, A. Sawa, T. Manako, H. Sato, H. Akoh, M. Kawasaki, and Y. Tokura, *Jpn. J. Appl. Phys.* **42**, L369 (2003).

[15] H. Tanaka, J. Zhang, and T. Kawai, *Phys. Rev. Lett.* **88**, 27204 (2002).

[16] M. Sugiura, K. Uragou, M. Noda, M. Tachiki, and T. Kobayashi, *Jpn. J. Appl. Phys.* **38**, 2675 (1999).

[17] N. Nakagawa, M. Asai, Y. Mukunoki, T. Susaki, and H. Y. Hwang, *Appl. Phys. Lett.* **86**, 082504 (2005).

[18] K. -J. Jin, H. -B. Lu, Q. -L. Zhou, K. Zhao, B. -L. Cheng, Z. -H. Chen, Y. -L. Zhou, and G. -Z. Yang, *Phys. Rev. B* **71**, 184428 (2005).

[19] C. M. Xiong, Y. G. Zhao, B. T. Xie, and P. L. Lang, *Appl. Phys. Lett.* **88**, 193507 (2006).

[20] C. Mitra, P. Raychaudhuri, K. Dorr, K.-H. Muller, L. Schultz, P.M. Oppeneer, and S.Wirth, *Phys. Rev. Lett.* **90**, 017202 (2003).

[21] J. R. Sun, B. G. Shen, H. F. Tian, J. Q. Li, and Y. X. Weng, *Appl. Phys. Lett.* **87**, 202502 (2005).

[22] A. T. Hanbicki, B. T. Jonker, G. Itskos, G. Kioseoglou, and A. Petrou, *Appl. Phys. Lett.* **80**, 1240 (2003).

[23] A. T. Hanbicki, O. M. J. van 't Erve, R. Magno, G. Kioseogloou, C. H. Li, B. T. Jonker, G. Itskos, G. Kioseoglou, and A. Petrou, *Appl. Phys. Lett.* **82**, 4092 (2003).

[24] C. H. Li, G. Kioseoglou, O. M. J. van 't Erve, A. T. Hanbicki, B. T. Jonker, R. Mallory, M. Yasar, and A. Petrou, *Appl. Phys. Lett.* **85**, 1544 (2004).

[25] H. Ohno, *Science* **281**, 951 (1998).

[26] Y. Ohno, D. K. Young, B. Beschoten, F. Matsukura, H. Ohno, and D. D. Awschalom, *Nature* **402**, 790 (1999).

[27] R. Fiederling, M. Keim, G. Reuscher, W. Ossau, G. Schmidt, A. Waag, and L. W. Molenkamp, *Nature* **402**, 787 (1999).

[28] B. T. Jonker, Y. D. Park, B. R. Bennett, H. D. Cheong, G. Kioseoglou, and A. Petrou, *Phys. Rev. B* **62**, 8180 (2000).

[29] V. Crisan, P. Entel, and G. Rollmann, *J. Magn. Magn. Mater.* **240**, 417 (2002).

[30] C. -Y. You and Y. Suzuki, *J. Magn. Magn. Mater.* **293**, 774 (2005).

[31] D. O. Demchenko and A. Y. Liu, *Phys. Rev. B* **73**, 115332 (2006).

[32] L. Esaki, P. J. Stiles, and S. von Molnar, *Phys. Rev. Lett.* **19**, 852 (1967).

[33] W. A. Thompson, T. Penney, F. Holtzberg, and S. Kirkpatrick, *Proc. 11th Int. Conf. Phys. Semicond.* **2**, 1255 (1972).

[34] G. Couturier, S. von Molnar, and W. Giriat, *J. Appl. Phys.* **62**, 3253 (1987).

[35] T. Siegrist, S. von Molnar, and F. Holtzberg, *Appl. Phys. Lett.* **47**, 1087 (1985).

[36] C. Kwon, M. C. Robson, K.-C. Kim, J. Y. Gu, S. E. Lofland, M. Bhagat, Z. Trajanovic, M. Rajeswari, T. Venkatesan, A. R. Kratz, R. D. Gomez, and R. Ramesh, *J. Magn. Magn. Mater.* **172**, 229 (1997).

[37] Y. Tokura, Y. Tomioka, H. Kuwahara, A. Asamitsu, Y. Moritomo, and M. Kasai, *J. Appl. Phys.* **79**, 5288 (1996).

[38] Z. Sroubek, *Phys. Rev. B* **2**, 3170 (1970).

[39] T. Susaki, N. Nakagawa, and H. Y. Hwang, *Phys. Rev. B* **75**, 104409 (2007).

[40] R. L. Anderson, *Solid-State Electron.* **5**, 341 (1962).

[41] L. J. van Ryuven, J. M. P Papenhuijzen, and A .C. Verhoeven, *Solid-State Electron.* **8**, 631 (1965).

[42] G. Gerra, A. K. Tagantsev, N. Setter, and K. Parlinski, *Phys. Rev. Lett.* **96**, 107603 (2006).

[43] C. T. Black and J. J. Welser, *IEEE Trans. Electron. Device* **46**, 776 (1999).

[44] C. S. Hwang, *J. Appl. Phys.* **92**, 432 (2002).

[45] D. W. Reagor, S. Y. Lee, Y. Li, and Q. X. Jia, *J. Appl. Phys.* **95**, 7971 (2004).

[46] J. Robertson and C. W. Chen, *Appl. Phys. Lett.* **74**, 1168 (1999)

[47] K. T. McCarthy, A. F. Hebard, and S. B. Arnason, *Phys. Rev. Lett.* **90**, 117201 (2003).

[48] I. Zutic, J. Fabian, and S. Das Sarma., *Phys. Rev. Lett.* **88**, 066603 (2002).

[49] H. Oheda, *Solid State Commun.* **33**, 203 (1980).

[50] H. Okamoto, H. Kida, T. Kamada, and Y. Hamakaawa, *Philos. Mag. B* **58**, 171 (1988).

[51] L. Fitting Kourkoutis, Y. Hotta, T. Susaki, H. Y. Hwang, and D. A. Muller, *Phys. Rev. Lett.* **97**, 256803 (2006).

[52] T. Yamamoto, S. Suzuki, K. Kawaguchi, and K. Takahashi, *Jpn. J. Appl. Phys.* **37**, 4737 (1998).

[53] M. Minohara, I. Ohkubo, H. Kumigashira, and M. Oshima, *Appl. Phys. Lett.* **90**, 132123 (2007).

[54] N. Furukawa *J. Phys. Soc. Japan* **66**, 2523 (1997).

[55] R. Tung, *Mater. Sci. Eng. R* **35**, 1 (2001).

[56] J. W. Freeland, J. J. Kavich, K. E. Gray, L. Ozyuzer, H. Zheng, J. F. Mitchell, M. P. Warusawithana, P. Ryan, X. Zhai, R. H. Kodama, and N. Ekstein, arXiv:cond-mat/0611112 (2006).

[57] G. Banach and W. M. Temmerman, *Phys. Rev. B* **69**, 054427 (2004).

[58] M. J. Calderon, L. Brey, and F. Guinea, *Phys. Rev. B* **60**, 6698 (1999).

[59] H. Zenia, G. A. Gehring, G. Banach, and W. M. Temmerman, *Phys. Rev. B* **71**, 024416 (2005).

[60] Y. Konishi, Z. Fang, M. Izumi, T. Manako, M. Kasai, H. Kuwahara, M. Kawasaki, K. Terakura, and Y. Tokura, *J. Phys. Soc. Japan* **68**, 3790 (1999).

[61] A. Ohtomo and H. Y. Hwang, *Nature* **427**, 423 (2004).

[62] N. Nakagawa, H. Y. Hwang, and D. A. Muller, *Nat. Mater.* **5**, 204 (2006).